

1      **Thermal and Rheological Structure of Lithosphere beneath Northeast China**

2                    Dong Yan<sup>1</sup>, You Tian<sup>1,2\*</sup>, Dapeng Zhao<sup>3</sup>, Hongli Li<sup>1</sup>

3      1. College of Geoexploration Science and Technology, Jilin University, Changchun 130026,

4                    China

5      2. Changbai Volcano Geophysical Observatory, Ministry of Education, Changchun 130026,

6                    China

7      3. Department of Geophysics, Graduate School of Science, Tohoku University, Sendai

8                    980-8578, Japan

9

10     Corresponding author: You Tian (tianyou@jlu.edu.cn)

11

12   **Key Points:**

- A 3-D model of lithospheric thermal structure and rheological strength beneath Northeast China is presented.
- Small-scale temperature changes and thermal lithosphere thickness variations between different tectonic blocks are revealed.
- The “crème brûlée” model can explain the lithospheric deformation in Northeast China.

19

20   **Abstract**

21     We investigate the 3-D lithospheric thermal and rheological structures beneath  
22   Northeast China using detailed P- and S-wave velocity models following mineral  
23   physics as well as geothermal methods. Small-scale temperature changes and thermal  
24   lithosphere thickness variations between different tectonic blocks are revealed. Our  
25   results show that strong lateral heterogeneities exist in the lithospheric thermal  
26   structure and rheological structure on both sides of the North-South Gravity  
27   Lineament (NSGL). The Changbai volcanic area and the central part of the Songliao

28 Basin in the eastern side of the NSGL exhibit higher temperatures, thinner thermal  
29 lithosphere and lower rheological strength, which are closely associated with the  
30 western Pacific plate subduction under the Eurasian continent, resulting in upwelling  
31 of wet and hot asthenospheric material above the stagnant Pacific slab in the mantle  
32 transition zone. The thermo-chemical erosion of the upwelling asthenospheric  
33 material may induce delamination of partial lithosphere under the Songliao Basin. In  
34 addition, the Songliao Basin edge is characterized by lower temperature, thicker  
35 thermal lithosphere and higher rheological strength, which may indicate a relatively  
36 stable lithosphere. The Halaha and Abaga volcanic areas in the western side of the  
37 NSGL exhibit higher temperature, thinner thermal lithosphere and lower rheological  
38 strength, which could be caused by small-scale upwelling of hot asthenospheric  
39 material associated with delamination of partial lithosphere beneath the Songliao  
40 Basin.

41

## 42 Plain Language Summary

43 We determine a 3-D model of lithospheric thermal and rheological structure  
44 under Northeast China to better understand the lithospheric destruction mechanism.  
45 Small-scale thermal and rheological structures between different tectonic blocks are  
46 revealed. There are significant lateral differences in the 3-D model between two sides  
47 of the North-South Gravity Lineament (NSGL), which serves as a vital tectonic  
48 boundary in eastern China. In the east of the NSGL, the Changbai volcano and the  
49 central part of the Songliao Basin show higher temperatures, thinner thermal  
50 lithosphere and lower rheological strength, which may be associated with upwelling  
51 of wet and hot asthenospheric material induced by the western Pacific plate  
52 subduction under the Eurasian plate. The thermo-chemical erosion of the ascending  
53 asthenospheric material could induce partial lithosphere beneath the Songliao Basin to  
54 sink into the upper mantle, leading to small-scale upwelling of asthenospheric  
55 material and providing magmas to the Halaha and Abaga volcanoes in the west of the  
56 NSGL. The edge of the Songliao Basin exhibits lower temperature, thicker thermal  
57 lithosphere and higher rheological strength, which may indicate a relatively stable

58 lithosphere.

59

## 60 1. Introduction

61 Northeast China is situated between the Sino-Korean Craton and the Siberian  
62 Plateau, facing the Japan Sea to the east (Figure 1). It is generally believed that in the  
63 early Mesozoic, Northeast China collided with North China along the Solonker suture  
64 zone (Sengor et al., 1993). During the late Mesozoic to Cenozoic, extensional  
65 structures had been widely developed in eastern China due to the combined effects of  
66 the Mongolia-Okhotsk Ocean closure and the westward subduction of the Pacific  
67 plate (Wang et al., 2006; Xu et al., 2013; Guo et al., 2018), which contributed to the  
68 formation of widespread extensional basins and orogenic belts, resulting in the nearly  
69 NE- and NNE-trending tectonic patterns of Northeast China at present (Figure 1).

70 The complex tectonic pattern of Northeast China has been extensively  
71 investigated in the past decades, and researchers have proposed several mechanisms  
72 to explain its tectonic evolution. Some workers have suggested that the widespread  
73 tectonic deformation and lithospheric thinning of Northeast China are associated with  
74 the western Pacific plate subduction or the closure of the Okhotsk Ocean (e.g., Ren et  
75 al., 2002; Meng et al., 2003; Zhao et al., 2004). A few other studies have shown that  
76 the subduction of the Pacific plate and the Philippine Sea plate contributed to the  
77 formation and development of the western Pacific marginal basins and Mesozoic  
78 basins in eastern China, resulting in strong lateral heterogeneity in the lithosphere (Li  
79 et al., 2012; Li et al., 2013). Xu et al. (2013) suggested that the tectonic evolution of  
80 Northeast China was mainly affected by the closure of the Mongolia-Okhotsk Ocean  
81 from the Jurassic to early Cretaceous, whereas the strong volcanic activities during  
82 the late Cretaceous were primarily related to the Paleo-Pacific plate subduction.

83 Many previous studies have investigated the seismic velocity structure beneath  
84 Northeast China (e.g., Pan et al., 2014; Guo et al., 2016; Kang et al., 2016; Tian et al.,  
85 2017; Guo et al., 2018; Ma et al., 2018; Tian et al., 2019; Jia et al., 2022), but there  
86 have been few studies of the thermal and rheological structure beneath this region.  
87 The study on the lithospheric thermal structure is mainly about the lithospheric

88 temperature distribution as well as variations of the thermal lithosphere thickness, and  
89 the lithospheric rheological structure is mainly described by two recognized  
90 rheological models: the jelly sandwich model (Ranalli & Murphy, 1987) and the  
91 crème brûlée model (Jackson, 2002). The conventional jelly sandwich model is based  
92 on rock mechanics results, suggesting that a weak ductile layer at the bottom of the  
93 lower crust separates the relatively strong upper crust and the uppermost mantle. In  
94 addition, the uppermost mantle contributes most to the lithospheric strength. This  
95 prevailing model had been used for almost two decades before the crème brûlée  
96 model was put forward. The new model is based on the depth distribution of  
97 seismicity, suggesting that a relatively strong crust underlain by a weak mantle and  
98 continental tectonic activities are controlled by the strength that is primarily  
99 distributed in the crust.

100 An and Shi (2006) studied the 3-D temperature structure at depths of 70-240 km  
101 beneath Mainland China using a shear wave velocity (Vs) model (CN03S) and  
102 estimated the thermal lithosphere thickness by considering the mantle adiabatic  
103 temperature at 1300°C. Sun et al. (2013) investigated the lithospheric temperature  
104 structure beneath the Chinese continent by solving the 3-D steady-state heat  
105 conduction equation using the finite element simulation. Deng and Tesauro (2016)  
106 investigated the thermal structure of the Chinese continental lithosphere by using the  
107 crustal temperature model of Sun et al. (2013) and the Vs model of Li et al. (2013). As  
108 a result, Deng and Tesauro (2016) obtained a lithospheric strength model of Mainland  
109 China. Although these previous studies have addressed the thermal and rheological  
110 structure of some representative tectonic blocks, their results could not reveal  
111 small-scale lateral variations of the lithospheric temperature and rheological strength  
112 under Northeast China due to the limited resolution of the previous models.

113 It is well recognized that temperature is a critical parameter in geodynamic  
114 studies because geodynamic and rheological processes in the mantle are mainly  
115 controlled by temperature (An & Shi, 2006, 2007). Furthermore, rheological  
116 properties of the lithosphere play an important role in controlling the tectonic  
117 deformation and geological evolution processes (Burov, 2011; Ranalli & Adams,

118 2013). Therefore, it is of great significance to clarify the spatial variation of  
119 lithospheric thermal structure and rheological strength beneath Northeast China to  
120 better understand its lithospheric deformation, intraplate volcanism and mantle  
121 dynamics.

122 In this work, we determine a new 3-D model of lithospheric thermal structure and  
123 rheological strength beneath Northeast China, which reveals many small-scale  
124 features of lithospheric structure of the region. The thermal lithosphere thickness in  
125 this region is determined from the 1300°C isotherm of the mantle adiabatic  
126 temperature. In addition, we analyze the relationship between the lithospheric strength  
127 and seismicity of the study region. The present results provide new constraints on the  
128 tectonic evolution process as well as the destruction mechanism of the continental  
129 lithosphere under Northeast China.

130

## 131 **2. Geological and Tectonic Settings**

132 Northeast China is bounded in the south by the Solonker suture zone, and in the  
133 north by the Mongolia-Okhotsk suture zone. Northeast China consists of several  
134 continental microplates, including the Erguna block and Xing'an block in the west, the  
135 Jiamusi block in the east, and the Songliao block in the middle (Wu et al., 1995; Zhou  
136 & Wilde, 2013; Zhang et al., 2014). The Xing'an block primarily consists of the Great  
137 Xing'an Range where widespread late Mesozoic volcanic rocks exist (Xu et al., 2013).  
138 The Songliao block is mainly composed of the Great and Lesser Xing'an Ranges in  
139 the southwest and northeast, respectively, the Songliao Basin in the center and the  
140 Zhangguangcai Range in the east (Wang & Li, 2018). In the late Mesozoic, the  
141 western Pacific plate subduction led to the accretion of the Nadanhada Terrane and the  
142 Jiamusi Block along the East Asian continental margin. During this period the crustal  
143 deformation is characterized by the formation of some NNE-trending faults in parallel  
144 with the continental margin. One of the major faults is the Tanlu fault zone, which  
145 branches into the Yilan-Yitong fault and the Dunhua-Mishan fault. The Yilan-Yitong  
146 fault has developed as an internal fault in the Songnen-Zhangguangcai Range Massif,  
147 separating the Songliao Basin and the Zhangguangcai Range. The Dunhua-Mishan

148 fault has served as a tectonic boundary between the Nadanhada Terrane and the  
149 Xingkai Massif (Xu et al., 2017).

150 During the late Mesozoic to Cenozoic, widespread tectonic deformations  
151 occurred in Northeast China, resulting in lithospheric thinning and intensive  
152 magmatic activities. In addition, widespread rifting and extensional basins have  
153 formed along the large-scale strike-slip faults (Griffin et al., 1998; Ren et al., 2002;  
154 Zhu et al., 2011; Zhang et al., 2014), including the Erlan Basin, the Hailar Basin and  
155 the Songliao Basin, which are mostly filled with several kilometers of lacustrine  
156 sediments. The Songliao Basin is the largest and an oil-producing basin, which has  
157 made prominent contributions to the oil and gas production for decades (Wang et al.,  
158 2001).

159 The Songliao Basin has a typical double-base structure. Its lower base is  
160 composed of late Jurassic and early Cretaceous rifting basins, which were filled with  
161 pyroclastic rocks and lacustrine sediments. Its upper base consists of widespread  
162 depressions, in which the lacustrine and delta sedimentary systems were formed  
163 during the late Cretaceous, and alluvial fans as well as fluvial strata were deposited  
164 during the Eocene and Neogene (Ren et al., 2002). Cenozoic volcanic rocks are  
165 distributed extensively in the rift valleys and ridges at edges of the Songliao Basin  
166 (Liu et al., 2001). Some of the best-known volcanic centers in Northeast China  
167 include the Changbai, Longgang, Jingpohu and Wudalianchi volcanoes (Figure 1).  
168 Therefore, Northeast China is an ideal natural laboratory to investigate the Cenozoic  
169 intraplate volcanism.

170 The North-South Gravity Lineament (NSGL), extending more than 3500 km from  
171 Northeast China to South China, serves as a vital tectonic boundary within mainland  
172 China (Figure 1). This lineament is generally parallel to the Tanlu fault zone and it  
173 passes through many important tectonic units in eastern China, including the NCC,  
174 the Dabie orogen, and the Yanshan orogen. The surface topography, the thicknesses  
175 of the crust and lithosphere, and the Bouguer gravity anomalies all change  
176 dramatically across the NSGL, indicating that it is an important physical boundary in  
177 eastern China (Menzies & Xu, 1998; Niu, 2005). Analysis of Sr-Nd-Os isotope data

178 for mantle xenoliths extracted from two sides of the NSGL show that it is also a  
179 geochemical boundary that separates two distinct mantle domains formed in different  
180 geological periods (Xu, 2007). Yang et al. (2005) investigated the crustal and  
181 lithospheric geophysical characteristics on both sides of the NSGL using seven  
182 geoscience transects. They suggested that the interactions of the Eurasian plate, the  
183 Indian plate and the Pacific plate, as well as mantle flow at the East Asian continent  
184 margin contributed to the crust-mantle structure on both sides of the gravity lineament.  
185 Xu (2007) suggested that the western Pacific plate subduction under the Eurasian  
186 continent has caused the lithospheric thinning with varying degrees beneath the  
187 western and eastern NCC, which may be a critical factor in the formation of the  
188 NSGL. In addition, the upwelling of asthenospheric material induced by dehydration  
189 of the stagnant Pacific slab in the mantle transition zone may further accelerate the  
190 formation of the NSGL (e.g., Zhao et al., 2004, 2009; Lei & Zhao, 2005; Huang &  
191 Zhao, 2006; Tian et al., 2009; Xu & Zhao, 2009). However, there is still no consensus  
192 on the formation mechanism of the NSGL to date. Therefore, it is of great significance  
193 to get further insight into the geophysical characteristics on both sides of the NSGL in  
194 Northeast China to better understand its formation and tectonic evolution mechanism.

195

### 196 **3. Data and Method**

#### 197 **3.1. Seismic Velocity Models**

198 The temperature distribution of the lithosphere is commonly estimated by solving  
199 the heat conduction equation with heat flow data, because heat conduction is the  
200 major transmission mode of thermal energy in the lithosphere. A number of  
201 geothermal studies have been made for North China (e.g., Zang et al., 2002a; He,  
202 2014; Huang et al., 2015; Zhang et al., 2016). However, the scarcity and uncertainty  
203 of heat flow data in Northeast China have hindered the estimation of lithospheric  
204 temperature distribution. In the present work, we study the 3-D temperature structure  
205 of the upper mantle at depths of 50-200 km beneath Northeast China using the robust  
206 3-D P- and S-wave velocity ( $V_p$ ,  $V_s$ ) models of Ma et al. (2018) and Shen et al. (2016)  
207 (see Figures S1 and S2 in Supporting Information) following a mineral physics

208 approach (Goes et al., 2000; Deschamps et al., 2002; An & Shi, 2006; Yang et al.,  
209 2013; Yan et al., 2019), which is described in detail in the Appendix.

210 The 3-D Vp model was determined by applying the joint inversion method of  
211 Zhao et al. (1992, 1994) to a great number of arrival-time data of local and regional  
212 earthquakes as well as relative travel-time residuals of teleseismic events (Ma et al.,  
213 2018). A 3-D ray-tracing technique by Zhao et al. (1992) was used to calculate  
214 theoretical travel times and ray paths. Depth variations of the Moho discontinuity  
215 were taken into account to improve the computing accuracy. The LSQR algorithm of  
216 Paige & Saunders (1982) was used to solve the large but sparse system of observation  
217 equations. Resolution tests showed that the lateral resolution of the 3-D Vp model is  
218 ~100 km beneath most parts of the study region.

219 The 3-D Vs model was obtained by ambient noise Rayleigh wave tomography  
220 using data recorded at 2073 seismic stations of multiple networks in China and  
221 earthquake surface wave tomography beneath the NECESS array in Northeast China  
222 (Shen et al., 2016). The same quality control procedures were applied to all data. The  
223 3-D Vs model was produced by a Bayesian Monte Carlo inversion on a  $0.5^\circ \times 0.5^\circ$  grid  
224 across the study region.

225 The high-resolution 3-D Vp and Vs models show similar velocity anomaly  
226 patterns except beneath some areas of the Erguna block where the distribution of  
227 seismic stations is sparse. Many significant tectonic and geological features in the  
228 lithosphere beneath Northeast China are revealed by the Vp and Vs models (Figure S1  
229 and Figure S2). In the western side of the NSGL, some low-Vp and low-Vs anomalies  
230 exist beneath the Halaha and Abaga volcanic areas. In the eastern side of the NSGL,  
231 prominent low-Vp and low-Vs zones at depths of 50-200 km are visible beneath the  
232 Cenozoic volcanic areas such as Changbai, Longgang and Jingpohu, which are in  
233 good agreement with many previous tomographic results (e.g., Zhao et al., 2004, 2009;  
234 Zhao & Tian, 2013; Tian et al., 2016, 2019; Guo et al., 2016, 2018). Significant  
235 high-Vp and high-Vs anomalies appear at edges of the Songliao Basin, and low-Vp  
236 and low-Vs anomalies are visible under the central part of the Songliao Basin, which  
237 are consistent with the previous seismic results (e.g., Guo et al., 2016, 2018).

238     **3.2. Lithospheric Temperature Estimation**

239     We adopt the high-resolution 3-D Vp and Vs models described above and use a  
240     global enumeration algorithm to invert seismic velocities for 3-D temperature  
241     structure of the upper mantle at depths of 50-200 km. To obtain a more accurate  
242     inversion result, we conduct a joint inversion of the Vp and Vs models to constrain  
243     the 3-D temperature structure of the upper mantle beneath Northeast China. The  
244     average annual surface temperature ( $\sim 10^{\circ}\text{C}$ ) and the inverted temperature values at 50  
245     km depth are adopted as the top and bottom boundary conditions, respectively, and  
246     the lithospheric temperature distribution above this depth (50 km) is estimated by  
247     solving the 1-D steady-state heat conduction equation. The sedimentary layer is not  
248     taken into account in our stratified crust model, because the average sediment  
249     thickness in Northeast China is less than 1 km according to the CRUST 1.0 model  
250     (<https://igppweb.ucsd.edu/~gabi/crust1.html>) and some previous studies (Laske et al.,  
251     2013; Tao et al., 2014). The stratified crust model is built with  $Vp < 6.2 \text{ km/s}$  for the  
252     upper crust, and for the middle crust with  $Vp$  of 6.2-6.5 km/s. The bottom boundary of  
253     the crust is determined by referring to the receiver function results of Zhang et al.  
254     (2020) and the CRUST 1.0 model.

255     The thermal conductivity is taken as  $k = k_0(1 + cz)(1 + b(T - 273.15))^{-1}$  in  
256     the crust (Chapman, 1986) and  $k = 0.368 \times 10^{-9} \times T^3 + (0.174 + 0.000265 \times$   
257      $T)^{-1}$  in the lithospheric mantle (Doin & Fleitout, 1996). Here  $k_0$  is measured  
258     thermal conductivity at zero temperature and one atmosphere pressure, which is  
259     assumed to be 3.0, 2.8 and 2.6  $\text{W}\cdot\text{m}^{-1}\cdot\text{K}^{-1}$  for the upper, middle and lower crust,  
260     respectively. The temperature coefficient  $b$  is taken as  $1.5 \times 10^{-3}$ ,  $0.8 \times 10^{-4}$  and  $1.5 \times$   
261      $10^{-4} \text{ K}^{-1}$  for the upper, middle and lower crust, respectively. The pressure coefficient  $c$   
262     is equal to  $1.5 \times 10^{-3} \text{ km}^{-1}$  for the whole crust.  $T$  is temperature (in Kelvin) at a depth  
263     of  $z$  (in km)

264     The heat production distribution in a stratified crust model is obtained by using  
265     the empirical relationship between P-wave velocity ( $V_P^0$ ) and the heat production ( $A$ )  
266     proposed by Rybach & Buntebarth (1984):

267                           $\ln A = 13.7 - 2.17V_P^0 \quad (293.15 \text{ K}, 100 \text{ MPa}) \quad (1)$

268 It is an effective method to estimate the heat production when heat flow data and  
269 radioactive element abundance data are sparse in a study region. However, the  $V_P$  in  
270 the deep earth is the in-situ velocity, which could considerably differ from the  
271 laboratory condition. Thus, it has to be corrected to the experimental reference  
272 conditions (293.15 K, 100 MPa) according to the following formula (Rybáček and  
273 Buntebarth, 1984; Sun et al., 2013):

274 
$$V_P^0 = V_P + (293.15 - T) \frac{\partial V_P}{\partial T} + (100 - P) \frac{\partial V_P}{\partial P} \quad (2)$$

275 where  $V_P$  is P-wave velocity at specific temperature  $T$  and pressure  $P$  (assumed to  
276 be lithostatic pressure). The temperature and pressure derivatives for each layer of the  
277 stratified crust model are listed in Table S1 in the Supporting Information.  
278 Nevertheless, the calculated heat production is high beneath some areas in the shallow  
279 part of the upper crust due to the low  $V_P$ , thus it is more appropriate to consider the  
280 heat production within the upper crust as a constant, which is assumed to be 1.25  
281  $\mu\text{W}\cdot\text{m}^{-3}$  in this study (Chi & Yan, 1998; Zang et al., 2002a). For the lithospheric  
282 mantle, a uniform heat production of 0.03  $\mu\text{W}\cdot\text{m}^{-3}$  is adopted (Rudnick et al., 1998;  
283 Wang, 2001).

284 **3.3. Lithospheric Strength Estimation**

285 The rheological structure of the lithosphere changes in space and time as a  
286 function of diverse factors, in particular, temperature, rock compositions, and pore  
287 fluid pressure (Ranalli, 2000). There are three main mechanisms for the lithospheric  
288 rheology, i.e., frictional sliding, brittle fracture and ductile creep (Kirby, 1983;  
289 Kohlstedt et al., 1995; Zang et al., 2007). Some previous studies have shown that in  
290 the shallow parts of the lithosphere with a low temperature, the dominant mechanism  
291 is the rock brittle deformation (frictional sliding and brittle fracture), whereas at  
292 greater depths with a high temperature, rocks predominantly deform by the ductile  
293 creep mechanism (Tesauro et al., 2012, 2015). In addition, frictional sliding mainly  
294 occurs in the upper crust, whereas brittle fracture takes place primarily in the lower  
295 crust and the uppermost mantle (Zang et al., 2007).

296 Frictional sliding depends linearly on pressure, which is independent of

297 temperature and strain rate (Pauselli et al., 2010). The Byerlee's law is widely  
298 accepted as the criterion for describing the frictional sliding along brittle faults in the  
299 crust, because the law was proposed based on experimental data (Byerlee, 1978),  
300 which can be expressed as:

301 
$$\sigma_f = f \rho g z (1 - \lambda) \quad (3)$$

302 where  $f$  is a numerical factor related to the fault type, being 3.0, 1.2 and 0.75 for  
303 thrust faulting, strike-slip faulting and normal faulting, respectively.  $\rho$  represents the  
304 average density of rocks above depth  $z$ ,  $g$  is the acceleration due to gravity, and  $\lambda$  is  
305 the pore fluid factor (ratio of pore fluid pressure to lithostatic pressure). In this study,  
306 we use the frictional sliding formula under the strike-slip faulting condition ( $f = 1.2$ )  
307 to calculate the lithospheric strength, because the faults in Northeast China are  
308 dominated by NNE-trending strike-slip motions (Ren et al., 2002; Xu et al., 2017).

309 However, in most of the previous studies, only the frictional sliding and ductile  
310 creep mechanisms were considered, whereas the brittle fracture was ignored because  
311 there was no appropriate way to do that, leading to an increase in the magnitude of  
312 rheological strength calculated. In this study, we take the brittle fracture mechanism  
313 into consideration in the process of calculating the rock strength in the lithosphere  
314 according to the empirical formula given by Zang et al. (2007):

315 
$$\sigma_b = B_0 \left[ 1 + K \left( \frac{\sigma_c}{B_0} \right)^m \right] \left[ 1 + \alpha \left( \lg \frac{T}{T_0} \right)^\beta \right] \left[ 1 + \gamma \lg \left( \frac{\dot{\varepsilon}}{\dot{\varepsilon}_0} \right) \right] \quad (4)$$

316 where  $B_0$ ,  $K$ ,  $m$ ,  $\alpha$ ,  $\beta$  and  $\gamma$  are empirical failure parameters that are listed in  
317 Table S2,  $\sigma_c$  denotes confining pressure that equals to lithostatic pressure,  $T$  is the  
318 temperature in Kelvin,  $T_0$  is the room temperature (298.15 K),  $\dot{\varepsilon}$  and  $\dot{\varepsilon}_0$  ( $10^{-5} \text{ s}^{-1}$ )  
319 are strain rate and reference strain rate, respectively. Previous studies have suggested  
320 that there is little difference in the rheological strength obtained by using the constant  
321 strain rate and observed strain rate from GPS observations (Zang et al., 2005; Tesauro  
322 et al., 2015; Deng & Tesauro, 2016). In this study, we calculate the lithospheric  
323 strength using the global average strain rate of  $10^{-15} \text{ s}^{-1}$ .

324 The creep strength of the lithosphere is generally described by power law  
325 (Weertman, 1970; Kohlstedt et al., 1995). We can calculate the lithospheric creep

326 strength according to the following equation:

$$327 \quad \sigma_d = \left( \frac{\dot{\varepsilon}}{C} \right)^{\frac{1}{n}} \exp \left( \frac{Q}{nRT} \right) \quad (5)$$

328 where  $\dot{\varepsilon}$  is the strain rate,  $C$ ,  $n$  and  $Q$  are material creep parameters independent  
329 of temperature and pressure, which represent the flow parameter, stress exponent and  
330 activation enthalpy, respectively,  $R$  is the gas constant, and  $T$  is the temperature in  
331 Kelvin. Previous studies have shown that the lithospheric rheological models can be  
332 divided into the soft rheology model and the hard rheology model according to the  
333 rock composition (Ranalli, 2000; Pauselli et al., 2010; Deng & Tesauro, 2016). A soft  
334 rheology is assumed to be controlled by felsic granulite and wet peridotite in the  
335 lower crust and the lithospheric mantle, respectively, whereas a hard rheology is  
336 controlled by mafic granulite and dry peridotite in the lower crust and the lithospheric  
337 mantle, respectively (Pauselli et al., 2010). Furthermore, a wet lithospheric mantle  
338 model is more suitable for areas that have been influenced recently by oceanic plate  
339 subduction and tectonic thermal events, whereas a dry lithospheric mantle might be  
340 more relevant for old and stable regions (Afonso & Ranalli, 2004). Northeast China  
341 has experienced multi-stage tectonic thermal events since the late Mesozoic to the  
342 Cenozoic. Hence, it is more suitable to choose the soft rheological model to study the  
343 lithospheric strength of Northeast China. The rheological parameters for lithospheric  
344 materials in this study are listed in Table S3.

345 In any depth range, rocks tend to deform by the dominant mechanism that  
346 exhibits the lowest strength (Kirby et al., 1991, 1996; Zang et al., 2007), and the  
347 rheological strength of the lithosphere at a specific depth is generally described by the  
348 yield strength envelop (YSE), which describes the maximum rock strength as a  
349 function of depth (Goetze & Evans, 1979). The integrated lithospheric strength ( $\sigma_L$ ) is  
350 estimated by vertical integration of the YSE as follows:

$$351 \quad \sigma_L = \int_0^H \text{YSE } dz \quad (6)$$

352 where  $H$  is the lithospheric thickness, and  $z$  is depth.

353

#### 354 4. Results and Discussion

355     **4.1. Lithospheric Temperature Structure**

356     In this study, we investigate the 3-D temperature (T) structure of the upper mantle  
357     at depths of 50-200 km from the Vp and Vs models described in Section 3.1 (Figure  
358     S3 and Figure S4). The T distributions estimated from the separate Vp and Vs models  
359     are similar to each other. Significant low-T zones exist beneath the Cenozoic volcanic  
360     areas. The edge of the Songliao Basin generally exhibits prominent low-T zones, and  
361     a relatively high-T zone appears under the central part of the Songliao Basin. The T  
362     distribution exhibits obvious differences in some areas of the Erguna block, which  
363     may be related to the discrepancy of Vp and Vs models due to the sparse distribution  
364     of seismic stations there. Figure 2 shows map views of the 3-D T structure obtained  
365     from the Vp and Vs joint inversion. Figure 3 shows eight vertical cross-sections of the  
366     3-D lithospheric temperature model. The lithospheric temperature distribution above  
367     50 km depth obtained by solving the 1-D steady-state heat conduction equation is  
368     displayed more clearly in Figure 4.

369     Our results reveal strong lateral heterogeneities in the lithospheric mantle beneath  
370     Northeast China. Significant high-T zones are visible at 50-200 km depths beneath the  
371     Halaha and Abaga volcanic areas in the western side of the NSGL (Figures 2, 3b, 3f  
372     and 3g). The two areas are characterized by relatively high-T zones in the middle and  
373     lower crust as well (Figures 4b, 4f and 4g). Some high-T zones exist beneath the  
374     Hailar Basin and the Erlian Basin (Figures 2c-2f, 3d and 3h). In the eastern side of the  
375     NSGL, prominent high-T zones exist at depths of 50-200 km beneath the Cenozoic  
376     volcanic areas such as Changbai, Longgang and Jingpohu (Figures 2, 3a-3c).  
377     Significant low-T zones appear at the edge of the Songliao Basin, and a prominent  
378     high-T zone is visible under the central part of the Songliao Basin (Figures 2, 3d and  
379     3e), which accord with the previous results obtained from other geophysical  
380     observations. For instance, surface heat flow data show that the central part of the  
381     Songliao Basin exhibits higher heat flow values and higher geothermal gradients  
382     (Wang, 2001; Wang & Cheng, 2011; Jiang et al., 2016). MT observations revealed  
383     prominent low-resistivity anomalies in the lithospheric mantle beneath the Changbai  
384     Volcano and the Songliao Basin (Han et al., 2018; Li et al., 2020). Significant high-T

385 anomalies are visible beneath the Tanlu fault zone and the Sanjiang Basin (Figure 2  
386 and Figure 3d-3f). The major geological tectonic units in Northeast China exhibit a  
387 NE-SW to NNE-SSW trending pattern, and the temperature anomalies in our results  
388 are generally consistent with this tectonic trend. Our results reveal some small-scale  
389 features of temperature variations between different tectonic blocks, as compared with  
390 the previous results (An & Shi, 2006, 2007; Sun et al., 2013; Deng et al., 2016).

#### 391 **4.2. Thickness of Thermal Lithosphere**

392 The thickness of thermal lithosphere beneath Northeast China (Figure 5) is  
393 estimated by considering the isothermal surface at 1300°C as its lower boundary  
394 (Artemieva & Mooney, 2001; An & Shi, 2006, 2007; He, 2014). The average thermal  
395 lithosphere thickness in the study region is approximately 100 km, which is consistent  
396 with the values determined by the previous studies (Wang, 2001; An & Shi, 2006;  
397 Wang & Cheng, 2011). Some small-scale variations in the thermal lithosphere  
398 thickness between the different tectonic blocks in Northeast China are revealed. The  
399 bottom boundary of the thermal lithosphere on the western and eastern sides of the  
400 NSGL changes dramatically, varying from ~80 km to more than 100 km depth. The  
401 thinnest thermal lithosphere (~60 km) occurs beneath the Changbai volcanic area.  
402 Other Cenozoic volcanic areas such as Longgang, Jingpohu and Halaha also exhibit a  
403 thinner thermal lithosphere (~70 km). The thermal lithosphere is relatively thin (~80  
404 km) beneath the central area of the Songliao Basin, the Sanjiang Basin and the  
405 Dunhua-Mishan fault. The thermal lithosphere is thick beneath the edge of the  
406 Songliao Basin, reaching ~120 km. These results are in good agreement with the  
407 thickness of seismic lithosphere obtained by some receiver function studies (Guo et  
408 al., 2014; Zhang et al., 2014). Previous studies have shown that the thickness  
409 difference between the seismic lithosphere and the thermal lithosphere is small in  
410 eastern China (Wang & Cheng, 2011; He, 2014), suggesting that our result is robust.

#### 411 **4.3 Lithospheric Strength Structure**

412 We further estimate the integrated lithospheric strength in Northeast China using  
413 the obtained 3-D temperature model (Figure 6). Four east-west vertical cross-sections  
414 of the lithospheric strength are shown in Figure 7, which indicate that the lithospheric

415 rheological strength coincides with the major tectonic features. As a whole, the  
416 lithosphere beneath the NSGL and the Songliao Basin edge exhibit a high strength  
417 (Figure 6). The lithospheric strength is very low beneath some Cenozoic volcanic  
418 areas such as Halaha, Abaga and Changbai (Figures 6, 7a and 7d). In addition, the  
419 lithospheric strength is generally low beneath some Cenozoic extensional basins, such  
420 as the Erlian Basin, the Sanjiang Basin and the central part of the Songliao Basin  
421 (Figures 6, 7c and 7d). The lithospheric strength is also low beneath the major fault  
422 zones, such as the Solonker-Xar Moron-Changchun-Yanji suture (SXCYS) and the  
423 Dunhua-Mishan fault (Figure 6).

424 Figure 8 shows yield strength envelops beneath six key areas in Northeast China.  
425 The upper crust predominantly deforms by frictional sliding, whereas brittle fracture  
426 becomes dominant in the upper part of the middle crust and even the lithospheric  
427 mantle. Both the Erlian Basin and the Hailar Basin exhibit a stronger middle crust but  
428 a very weak lower crust and upper mantle. The lithospheric strength values of the  
429 Songliao Basin and the Sanjiang Basin are similar to those of the Erlian Basin. The  
430 strength envelops in the Changbai and Halaha volcanic areas are characterized by a  
431 much stronger upper crust than the middle crust. A major difference between the  
432 strength profiles of the volcanic areas and the extensional basins is the existence of a  
433 weak middle crust beneath the volcanic areas. In addition, the ductile regime becomes  
434 more dominant in the upper crust beneath the volcanic areas than that beneath the  
435 extensional basins. In general, the lithospheric strength is primarily concentrated in  
436 the upper and middle crust (Figure 8), indicating that Northeast China deforms  
437 according to the “crème brûlée” model. The strength of the lower crust is relatively  
438 low, which may imply the presence of decoupling between the crust and the  
439 lithospheric mantle. The upper crust and the middle crust with a high rigidity are the  
440 major parts that bear the tectonic stress in the lithosphere.

#### 441 **4.4. Lithospheric Strength and Seismicity**

442 Seismicity is a good indicator for active tectonic deformation, because  
443 earthquakes are generally caused by brittle fracture of the lithospheric plate. Hence,  
444 there should be some links between seismicity and variations of the lithospheric

strength. We use the International Seismological Center (ISC) catalog that lists earthquakes occurring in Northeast China during 1970 to 2020 with  $M_b \geq 4.0$  to analyze the relationship between the lithospheric strength and crustal seismicity (see Figures 6 and 7). Most of the earthquakes occurred close to both sides of the NSGL where the lithospheric strength is higher or the areas characterized by sharp strength variations. These rigid areas are able to accumulate tectonic stress and liable to rupture under the effect of the stress. There exists a high concentration of crustal earthquakes in the central part of the Songliao Basin where the lithosphere exhibits a higher temperature and a lower rigidity. The crustal fluids would weaken the rocks and then trigger earthquakes (e.g., Mishra & Zhao, 2003; Huang & Zhao, 2004; Wei et al., 2013; Xia et al., 2020; Li et al., 2021). Some earthquakes occurred in the SXCYS and the Tanlu fault zone, which may be attributed to the tectonic stress associated with the strike-slip faulting. Swarms of deep-focus earthquakes ( $> 400$  km depth) occur actively beneath the Wangqing and Hunchun areas in Jilin province, which are located within the subducting Pacific plate (Zhang & Tang, 1983; Zhao & Tian, 2013; Jiang et al., 2015; Chen et al., 2017; Jiang et al., 2019). Most of the earthquakes in Northeast China occurred in the upper and middle crust and are restricted in a depth range of 10-20 km, where the lithospheric strength changes dramatically. In contrast, few earthquakes occurred in the lower crust characterized by a low rigidity, indicating that the lower crust is under a ductile condition.

#### 465 **4.5. Uncertainty Estimates**

466 We also investigate the effect of uncertainties of the 3-D velocity models on the  
467 temperature estimation. Although previous studies have indicated that the effect of  
468 mantle composition variation on the inverted temperature structure is very small  
469 (Nolet and Zielhuis, 1994; Sobolev et al., 1996; Goes et al., 2000), we investigate the  
470 relationship between temperature and Vp and Vs computed at 50 km depth for the  
471 on-cratonic mantle model (with olivine 83%, orthopyroxene 15% and garnet 2%)  
472 proposed by Shapiro & Ritzwoller (2004), as shown in Figure 9. In general,  
473 uncertainties in the mantle composition variation in the velocity-temperature (V-T)  
474 conversion are less than 1% for both Vp and Vs models, as compared with those from

475 the off-cratonic mantle model (blue lines in Figure 9), which are virtually negligible.

476 The anelastic parameters may not as well constrained by laboratory  
477 measurements as the elastic parameters of mantle minerals. Thus, the anelastic  
478 correction would contribute to the major part of uncertainty in the V-T conversion.  
479 Referring to Shapiro & Ritzwoller (2004), we investigate the relationship between  
480 temperature and Vp and Vs computed at 50 km depth through increasing  $A$  by 50%  
481 of the anelastic parameters (red lines in Figure 9). The Vp and Vs variations at 1500°C  
482 are roughly 2% and 6% respectively, but they are less than 1% at ~1300°C and  
483 1100°C. These results indicate that uncertainties resulting from the anelastic  
484 correction are large at high temperatures ( $> 1500^{\circ}\text{C}$ ), but can be ignored at lower  
485 temperatures ( $< 1100^{\circ}\text{C}$ ).

486 In this study, the effect of partial melt or the presence of fluids in the upper  
487 mantle is not taken into account because it has not been well constrained by  
488 experimental results so far, which may cause some uncertainties in the V-T conversion.  
489 In addition, the 3-D Vp and Vs models we used also have some uncertainties. The Vp  
490 and Vs uncertainties at depths  $< 120$  km are generally smaller than 0.1 km/s, which  
491 may cause a temperature variation of 50-130°C. The Vs uncertainties at depths greater  
492 than 120 km are mostly  $< 0.2$  km/s, which may cause a temperature variation of  
493 80-150°C. Although the uncertainties may be larger at high temperatures ( $> 1300^{\circ}\text{C}$ ),  
494 they have a negligible effect on the estimation of lithospheric strength because the  
495 temperature is well above the value ( $\sim 900^{\circ}\text{C}$ ) at which the lithospheric strength drops  
496 almost to zero (Ranalli, 1994; Jackson et al., 2002).

#### 497 **4.6. Tectonic Implications**

498 Combining the results of this work and many previous studies, we deem that the  
499 lithospheric structure under Northeast China is very heterogeneous. The Changbai  
500 volcanic area, the central part of the Songliao Basin and the Sanjiang Basin in the  
501 eastern side of the NSGL exhibit lower seismic velocity, higher temperature, thinner  
502 thermal lithosphere and lower lithospheric strength. In addition, these areas, in  
503 particular, the Songliao Basin, exhibit higher heat flows and larger geothermal  
504 gradients (Tian et al., 1992; Wang, 2001; Ren et al., 2002; Wang & Cheng, 2011; Xu

505 et al., 2013; Jiang et al., 2016). Hence, we think that the subduction of the (Paleo-)  
506 Pacific plate beneath the Eurasian plate since the late Mesozoic has resulted in  
507 ascending of wet and hot asthenospheric material in the big mantle wedge (BMW)  
508 above the Pacific slab that is stagnant in the mantle transition zone, leading to the  
509 long-term thermo-chemical erosion beneath these Cenozoic volcanic areas and  
510 extensional basins (e.g., Zhao et al., 2004, 2009; Lei & Zhao, 2005; Zhao & Tian,  
511 2013; Jia et al., 2022). The Tanlu fault system might serve as a channel for the  
512 upwelling of the wet and hot asthenospheric material and play an essential role in the  
513 destruction and thinning of the lithosphere in Northeast and eastern China during the  
514 Late Mesozoic to Cenozoic (e.g., Lei et al., 2020). The persistent thermo-chemical  
515 erosion of the upwelling asthenospheric material may induce the delamination of  
516 partial lithosphere beneath the Songliao Basin, resulting in a relatively thin thermal  
517 lithosphere beneath the central part of the basin. The basin edge is characterized by  
518 faster seismic velocity and stronger lithosphere, lower temperature and thicker  
519 thermal lithosphere, which may indicate a stable lithosphere that has not been  
520 delaminated. These features also suggest the strong lateral heterogeneity of the  
521 lithosphere beneath the Songliao Basin. The lithospheric delamination beneath the  
522 Songliao Basin might induce upwelling of the surrounding small-scale hot  
523 asthenospheric material, providing magmas to the Halaha and Abaga volcanoes in the  
524 western side of the NSGL (e.g., Wei et al., 2019; Jia et al., 2022). Hence, prominent  
525 high-T zones are visible beneath these areas. Summarizing all these results, we  
526 present a cartoon to describe the mantle structure and dynamics under Northeast  
527 China and the formation mechanism of the Cenozoic intraplate volcanism (Figure 10).

528

## 529 **5. Conclusions**

530 We use high-resolution 3-D P- and S-wave velocity models to investigate the  
531 thermal structure of the lithosphere in Northeast China and estimate the thermal  
532 lithosphere thickness from the 1300°C isotherm of the mantle adiabatic temperature.  
533 A rheological strength model of the lithosphere under Northeast China is also  
534 determined. The main results of this work are summarized as follows.

535 (1) The lithosphere beneath the Changbai volcanic area and the central part of the  
536 Songliao Basin is characterized by higher temperature, thinner thermal lithosphere  
537 and lower rheological strength, which are caused by the upwelling hot and wet  
538 asthenospheric material in the big mantle wedge above the subducting Pacific plate  
539 beneath East Asia.

540 (2) The Songliao Basin edge is characterized by lower temperature, thicker thermal  
541 lithosphere and higher rheological strength, indicating that the thermo-chemical  
542 erosion of the upwelling asthenospheric material may induce delamination of partial  
543 lithosphere under the Songliao Basin, but a relatively stable lithosphere may still  
544 remain under the basin edge.

545 (3) The Halaha and Abaga volcanic areas in the western side of the NSGL exhibit  
546 higher temperature, thinner thermal lithosphere and lower rheological strength, which  
547 may be caused by small-scale upwelling of hot asthenospheric material associated  
548 with the delamination of partial lithosphere beneath the Songliao Basin.

549 (4) The lithospheric strength is primarily concentrated in the crust beneath Northeast  
550 China, suggesting that the study region deforms according to the “crème brûlée”  
551 model.

552 (5) Most of the earthquakes in Northeast China take place in the upper and middle  
553 crust, indicating that the upper and middle crust is brittle and so bears the tectonic  
554 stress in the lithosphere.

555

## 556 **Appendix: Mineral Physics Approach**

557 The density ( $\rho_0$ ) and elastic moduli ( $K_0$  and  $\mu_0$ ) of common upper mantle  
558 minerals at normal temperature and pressure ( $T_0 = 300K, P = 0$ ) can be obtained  
559 through laboratory measurements (see Table S4). Then the density and elastic moduli  
560 of each mineral at a specific temperature  $T$  and zero pressure ( $P = 0$ ) are estimated  
561 using the following equations (Anderson, 1988; Duffy & Anderson, 1989; Vacher et  
562 al., 1998):

$$\rho(T, 0) = \rho_0 \exp \left[ - \int_{T_0}^T \alpha(T') dT' \right]$$

563  $\alpha(T) = a_0 + a_1T + a_2T^{-1} + a_3T^{-2}$  (A1)

564  $M(T, 0) = M_0 \left[ \frac{\rho(T, 0)}{\rho_0} \right]^{\delta_M}$

565  $\delta_M = -\frac{1}{\alpha M_0} \frac{\partial M}{\partial T}$  (A2)

566 where  $\rho_0$  and  $\rho(T, 0)$  are densities of lithospheric minerals at the normal and  
 567 specific temperatures, respectively,  $\alpha(T)$  is the coefficient of thermal expansion  
 568 (CTE),  $a_i(i = 0,1,2,3)$  represents parameters measured at the laboratory (see Table  
 569 S4),  $M$  is elastic modulus, and  $\delta_M$  is the Anderson-Grüneisen parameter.

570 Combining the Euler finite strain method and the third-order Birch-Murnaghan  
 571 isothermal equation of state (Birch, 1947; 1978), we have:

572  $P = -3K_{T,0}(1 - 2\varepsilon)^{5/2} \left[ \varepsilon + \frac{3}{2} \left( 4 - \frac{\partial K}{\partial P} \right) \varepsilon^2 \right]$  (A3)

573 where  $\varepsilon$  is the Euler strain that can be calculated by solving Eq. (A3) using the  
 574 pressure values from the PREM model (Dziewonski & Anderson, 1981). Then the  
 575 density and elastic moduli of each upper mantle mineral at a specific temperature and  
 576 pressure can be estimated with the following formulas (Deschamps et al., 2002):

577  $\rho(T, P) = \rho(T, 0)(1 - 2\varepsilon)^{3/2}$  (A4)

578  $K(T, P) = (1 - 2\varepsilon)^{\frac{5}{2}} (K_{T,0} + C_K \varepsilon)$

579  $C_K = 5K_{T,0} - 3K_{T,0} \frac{\partial K}{\partial P}$  (A5)

580  $\mu(T, P) = (1 - 2\varepsilon)^{\frac{5}{2}} (\mu_{T,0} + C_\mu \varepsilon)$

581  $C_\mu = 5\mu_{T,0} - 3K_{T,0} \frac{\partial \mu}{\partial P}$  (A6)

582 In this study, the off-cratonic mantle model (with olivine 68%, orthopyroxene  
 583 18%, clinopyroxene 11% and garnet 3%) proposed by Shapiro & Ritzwoller (2004) is  
 584 adopted, because Northeast China has experienced frequent tectonic events during the  
 585 late Mesozoic to Cenozoic. The density and elastic moduli of the upper mantle can be  
 586 calculated using the Voigt-Reuss-Hill method (Watt et al., 1976). Then the P- and  
 587 S-wave velocities can be determined using the following equations:

588  $V_P(T, P) = \sqrt{\frac{\bar{K}(T, P) + \frac{4}{3}\bar{\mu}(T, P)}{\bar{\rho}(T, P)}}$

589

$$V_S(T, P) = \sqrt{\frac{\bar{\mu}(T, P)}{\bar{\rho}(T, P)}} \quad (\text{A7})$$

590 Some previous studies have suggested that seismic velocity can be significantly  
 591 affected by anelasticity of the mantle as the depth increases (e.g., Karato & Spetzler,  
 592 1990; Karato, 1993). The effect of anelasticity on Vs is generally estimated with the  
 593 quality factor as follows (Anderson & Given, 1982; Goes et al., 2000):

594

$$Q_S(T, P, \omega) = A\omega^a \exp\left[\frac{a(H^* + PV^*)}{RT}\right] \quad (\text{A8})$$

595 where  $A$  and  $a$  are constants measured at laboratory,  $\omega$  is frequency,  $H^*$  and  $V^*$   
 596 are activation energy and activation volume, respectively, and  $R$  is gas constant.  
 597 Following Sobolev et al. (1996), we use  $A=0.148$ ,  $a=0.15$ ,  $H^*=500$  kJ·mol<sup>-1</sup>, and  
 598  $V^*=20$  cm<sup>3</sup>·mol<sup>-1</sup>. The P-wave quality factor can be expressed as (Anderson & Given,  
 599 1982):

600

$$Q_P(T, P, \omega) = (9/4)Q_S(T, P, \omega) \quad (\text{A9})$$

601 Thus, considering the anelastic effect, Vp and Vs can be expressed as (Minster &  
 602 Anderson, 1981; Goes et al., 2000; Cammarano et al., 2003):

603

$$V_P(T, P, \omega) = V_P(T, P) \left[ 1 - \frac{2}{9} \cot\left(\frac{\pi a}{2}\right) Q_S^{-1}(T, P, \omega) \right]$$

604

$$V_S(T, P, \omega) = V_S(T, P) \left[ 1 - \frac{1}{2} \cot\left(\frac{\pi a}{2}\right) Q_S^{-1}(T, P, \omega) \right] \quad (\text{A10})$$

605 The above-mentioned approach is a forward process, which can be used to invert for  
 606 the upper mantle temperature distribution with 3-D Vp and Vs models determined by  
 607 seismic tomography.

608

## 609 Acknowledgements

610 This work was supported by the National Natural Science Foundation of China  
 611 (grant No. 41874049), a grant from Japan Society for the Promotion of Science (grant  
 612 No. 19H01996) and Fundamental Research Funds for the Central Universities in  
 613 China. We appreciate the helpful discussions with Profs. Pengfei Zhao and Rongqiang  
 614 Wei. We used the Generic Mapping Tools (GMT) software package (Wessel & Smith,  
 615 1998) to plot most of the figures.

616

617 **Data Availability Statement**

618 The 3-D Vp model of Ma et al. (2018) and the obtained 3-D thermal and rheological  
619 strength models of the lithosphere beneath Northeast China are archived on the  
620 website: (<http://doi.org/10.6084/m9.figshare.19246236>). The list of crustal  
621 earthquakes ( $M_b \geq 4.0$ ) in Northeast China during 1970 to 2020 is available at the  
622 International Seismological Center (<http://www.isc.ac.uk/iscbulletin/search/catalogue>),  
623 which is also archived on the website above. The 3-D Vs model of Shen et al. (2016)  
624 is available at the website (<http://ciei.colorado.edu/Models>).

625

626 **References**

- 627 Afonso, J. C., & Ranalli, G. (2004). Crustal and mantle strengths in continental  
628 lithosphere: is the jelly sandwich model obsolete? *Tectonophysics*, 394, 221-232.  
629 <https://doi.org/10.1016/j.tecto.2004.08.006>
- 630 An, M., & Shi, Y. (2006). Lithospheric thickness of the Chinese continent. *Physics of*  
631 *the Earth and Planetary Interiors*, 159, 257-266.  
632 <https://doi.org/10.1016/j.pepi.2006.08.002>
- 633 An, M., & Shi, Y. (2007). Three-dimensional thermal structure of the Chinese  
634 continental crust and upper mantle. *Science in China*, 50, 1441-1451.  
635 <https://doi.org/10.1007/s11430-007-0071-3>
- 636 Anderson, D. L. (1988). Temperature and pressure derivatives of elastic constants  
637 with application to the mantle. *Journal of Geophysical Research*, 93, 4688-4700.  
638 <https://doi.org/10.1029/JB093iB05p04688>
- 639 Anderson, D. L., & Given, J. W. (1982). Absorption band Q model for the earth.  
640 *Journal of Geophysical Research*, 87, 3893-3904.  
641 <https://doi.org/10.1029/JB087iB05p03893>
- 642 Artemieva, I. M., & Mooney, W. D. (2001). Thermal thickness and evolution of  
643 Precambrian lithosphere: a global study. *Journal of Geophysical Research*, 106,  
644 16387-16414. <https://doi.org/10.1029/2000JB900439>
- 645 Birch, F. (1947). Finite elastic strain of cubic crystals. *Physical Review*, 71, 809-824.  
646 <https://doi.org/10.1103/PhysRev.71.809>

- 647 Birch, F. (1978). Finite strain isotherm and velocities for single-crystal and  
648 polycrystalline NaCl at high pressures and 300°K. *Journal of Geophysical*  
649 *Research*, 83, 1257-1268. <https://doi.org/10.1029/JB083iB03p01257>
- 650 Burov, E. B. (2011). Rheology and strength of the lithosphere. *Marine and Petroleum*  
651 *Geology*, 28, 1402-1443. <https://doi.org/10.1016/j.marpetgeo.2011.05.008>
- 652 Byerlee, J. D. (1978). Friction of rocks. *Pure and Applied Geophysics*, 116, 615-626.  
653 <https://doi.org/10.1007/BF00876528>
- 654 Cammarano, F., Goes, S., Vacher, P., & Giardini, D. (2003). Inferring upper-mantle  
655 temperatures from seismic velocities. *Physics of the Earth and Planetary*  
656 *Interiors*, 138, 197-222. [https://doi.org/10.1016/S0031-9201\(03\)00156-0](https://doi.org/10.1016/S0031-9201(03)00156-0)
- 657 Chen, C., Zhao, D., Tian, Y., Wu, S., Akira, H., Lei, J., et al. (2017). Mantle transition  
658 zone, stagnant slab and intraplate volcanism in Northeast Asia. *Geophysical*  
659 *Journal International*, 209, 68-85. <https://doi.org/10.1093/gji/ggw491>
- 660 Chi, Q., & Yan, M. (1998). Radioactive elements of rocks in North China platform  
661 and the thermal structure and temperature distribution of the modern continental  
662 lithosphere. *Chinese Journal of Geophysics*, 41, 38-48.
- 663 Deng, Y., & Tesauro, M. (2016). Lithospheric strength variations in Mainland China:  
664 Tectonic implications. *Tectonics*, 35, 2313-2333.  
665 <https://doi.org/10.1002/2016TC004272>
- 666 Deschamps, F., Trampert, J., & Snieder, R. (2002). Anomalies of temperature and iron  
667 in the uppermost mantle inferred from gravity data and tomographic models.  
668 *Physics of the Earth and Planetary Interiors*, 129, 245-264.  
669 [https://doi.org/10.1016/S0031-9201\(01\)00294-1](https://doi.org/10.1016/S0031-9201(01)00294-1)
- 670 Doin, M., & Fleitout, L. (1996). Thermal evolution of the oceanic lithosphere: an  
671 alternative view. *Earth and Planetary Science Letters*, 142, 121-136.  
672 [https://doi.org/10.1016/0012-821X\(96\)00082-9](https://doi.org/10.1016/0012-821X(96)00082-9)
- 673 Duffy, T. S., & Anderson, D. L. (1989). Seismic velocities in mantle minerals and the  
674 mineralogy of the upper mantle. *Journal of Geophysical Research*, 94,  
675 1895-1912. <https://doi.org/10.1029/JB094iB02p01895>
- 676 Dziewonski, A. M., & Anderson, D. L. (1981). Preliminary reference Earth model.

- 677        *Physics of the Earth and Planetary Interiors*, 25, 297-356.  
678        [https://doi.org/10.1016/0031-9201\(81\)90046-7](https://doi.org/10.1016/0031-9201(81)90046-7)
- 679        Goes, S., Govers, R., & Vacher, P. (2000). Shallow mantle temperature under Europe  
680        from P and S wave tomography. *Journal of Geophysical Research*, 105,  
681        11153-11169. <https://doi.org/10.1029/1999JB900300>
- 682        Goetze, C., & Evans, B. (1979). Stress and temperature in the bending lithosphere as  
683        constrained by experimental rock mechanics. *Geophysical Journal International*,  
684        59, 463-478. <https://doi.org/10.1111/j.1365-246X.1979.tb02567.x>
- 685        Griffin, W. L., Andi, Z., O'Reilly, S. Y., & Ryan, C. G. (1998). Phanerozoic evolution  
686        of the lithosphere beneath the Sino-Korean Craton. *Mantle Dynamics and Plate*  
687        *Interactions in East Asia*, 27, 107-126. <https://doi.org/10.1029/gd027p0107>
- 688        Guo, Z., Cao, Y., Wang, X., Chen, J. Y., Ning, J., He, W., et al. (2014). Crust and  
689        upper mantle structures beneath Northeast China from receiver function studies.  
690        *Earthquake Science*, 27, 265-275. <https://doi.org/10.1007/s11589-014-0076-x>
- 691        Guo, Z., Wang, K., Yang, Y., Tang, Y., Chen, J. Y., & Hung, S.-H. (2018). The origin  
692        and mantle dynamics of Quaternary intraplate volcanism in Northeast China  
693        from joint inversion of surface wave and body wave. *Journal of Geophysical*  
694        *Research: Solid Earth*, 123, 2410-2425. <https://doi.org/10.1002/2017JB014948>
- 695        Guo, Z., Chen, J. Y., Ning, J., Yang, Y., Afonso, J. C., & Tang, Y. (2016). Seismic  
696        evidence of on-going sublithosphere upper mantle convection for intra-plate  
697        volcanism in Northeast China. *Earth and Planetary Science Letters*, 433, 31-43.  
698        <https://doi.org/10.1016/j.epsl.2015.09.035>
- 699        Han, J., Guo, Z., Liu, W., Hou, H., Liu, G., Han, S., et al. (2018). Deep dynamic  
700        process of lithosphere thinning in Songliao basin. *Chinese Journal of Geophysics*,  
701        61, 2265-2279. <https://doi.org/10.6038/cjg2018L0155>
- 702        He, L. (2014). The Rheological boundary layer and its implications for the difference  
703        between the thermal and seismic lithospheric bases of the North China Craton.  
704        *Chinese Journal of Geophysics*, 57, 53-61. <https://doi.org/10.6038/cjg20140106>
- 705        Huang, F., He, L., & Wu, Q. (2015). Lithospheric thermal structure of the Ordos Basin  
706        and its implications to destruction of the North China Craton. *Chinese Journal of*

- 707        *Geophysics*, 58, 3671-3686. <https://doi.org/10.6038/cjg20151020>
- 708     Huang, J., & Zhao, D. (2004). Crustal heterogeneity and seismotectonics of the region  
709     around Beijing, China. *Tectonophysics*, 385, 159-180.
- 710     Huang, J., & Zhao, D. (2006). High-resolution mantle tomography of China and  
711     surrounding regions. *Journal of Geophysical Research*, 111, B09305.  
712     <https://doi.org/10.1029/2005JB004066>
- 713     Jackson, J. (2002). Strength of the continental lithosphere: time to abandon the jelly  
714     sandwich? *GSA Today*, 12, 4-9.  
715     [https://doi.org/10.1130/1052-5173\(2002\)012<0004:SOTCLT>2.0.CO;2](https://doi.org/10.1130/1052-5173(2002)012<0004:SOTCLT>2.0.CO;2)
- 716     Jia, R., Zhao, D., & Wu, J. (2022). P-wave anisotropic tomography of NE China:  
717     insight into lithospheric deformation, mantle dynamics and intraplate volcanism.  
718     *Geophysical Journal International*, 229, 1372-1391.  
719     <https://doi.org/10.1093/gji/ggab516>
- 720     Jiang, G., Gao, P., Rao, S., Zhang, L., Tang, X., Huang, F., et al. (2016). Compilation  
721     of heat flow data in the continental area of China (4<sup>th</sup> edition), *Chinese Journal  
722     of Geophysics*, 59, 2892-2910. <https://doi.org/10.6038/cjg20160815>
- 723     Jiang, G., Zhao, D., & Zhang, G. (2015). Detection of metastable olivine wedge in the  
724     western Pacific slab and its geodynamic implications. *Physics of the Earth and  
725     Planetary Interiors*, 238, 1-7. <https://doi.org/10.1016/j.pepi.2014.10.008>
- 726     Jiang, J., Chen, Q., & Jiao, L. (2019). Waveform detection and location of deep  
727     earthquakes in the subduction zone beneath Northeast China. *Chinese Journal of  
728     Geophysics*, 62, 2930-2945. <https://doi.org/10.6038/cjg2019M0210>
- 729     Kang, D., Shen, W., Ning, J., & Ritzwoller, M. H. (2016). Seismic evidence for  
730     lithospheric modification associated with intracontinental volcanism in  
731     Northeastern China. *Geophysical Journal International*, 204, 215-235.  
732     <https://doi.org/10.1093/gji/ggv441>
- 733     Karato, S. (1993). Importance of anelasticity in the interpretation of seismic  
734     tomography. *Geophysical Research Letters*, 20, 1623-1626.  
735     <https://doi.org/10.1029/93GL01767>
- 736     Karato, S., & Spetzler, H. A. (1990). Defect microdynamics in minerals and

- 737 solid-state mechanism of seismic wave attenuation and velocity dispersion in the  
738 mantle. *Reviews of Geophysics*, 28, 399-421.  
739 <https://doi.org/10.1029/RG028i004p00399>
- 740 Kirby, S. H. (1983). Rheology of the lithosphere. *Reviews of Geophysics*, 21,  
741 1458-1487. <https://doi.org/10.1029/RG021i006p01458>
- 742 Kirby, S. H., Durham, W. B., & Stern, L. A. (1991). Mantle phase changes and  
743 deep-earthquake faulting in subducting lithosphere. *Science*, 252, 216-225.  
744 <https://doi.org/10.1126/science.252.5003.216>
- 745 Kirby, S. H., Stein, S., Okal, E. A., & Rubie, D. C. (1996). Metastable mantle phase  
746 transformations and deep earthquakes in subducting oceanic lithosphere, *Reviews*  
747 *of Geophysics*, 34, 261-306. <https://doi.org/10.1029/96RG01050>
- 748 Kohlstedt, D. L., Evans, B., & Mackwell, S. J. (1995). Strength of the lithosphere:  
749 constraints imposed by laboratory experiments. *Journal of Geophysical Research*,  
750 100, 17587-17602. <https://doi.org/10.1029/95JB01460>
- 751 Laske, G., Masters, G., Ma, Z., & Pasyanos, M. (2013). Update on CRUST1.0 - A  
752 1-degree global model of Earth's crust. *EGU General Assembly Conference*  
753 *Abstracts*.
- 754 Lei, J., & Zhao, D. (2005). P-wave tomography and origin of the Changbai intraplate  
755 volcano in Northeast Asia. *Tectonophysics*, 397, 281-295.  
756 <https://doi.org/10.1016/j.tecto.2004.12.009>
- 757 Lei, J., Zhao, D., Xu, X., Du, M., Mi, Q., & Lu, M. (2020). P-wave upper-mantle  
758 tomography of the Tanlu fault zone in eastern China. *Physics of the Earth and*  
759 *Planetary Interiors*, 299, 106402. <https://doi.org/10.1016/j.pepi.2019.106402>
- 760 Li, H., Liu, C., Tian, Y., Wu, Z., & Zhu, H. (2021). Seismic tomography of the  
761 Songyuan area, Northeast China: constraints on seismogenic structure. *Chinese*  
762 *Journal of Geophysics*, 64, 1597-1607. <https://doi.org/10.6038/cjg2021O0288>
- 763 Li, S., Weng, A., Li, J., Shan, X., Han, J., Tang, Y., et al. (2020). Deep origin of  
764 Cenozoic volcanoes in Northeast China revealed by 3-D electrical structure.  
765 *Science China (Earth Sciences)*, 63, 533-547.  
766 <https://doi.org/10.1007/s11430-018-9537-2>

- 767 Li, S., Zhao, G., Dai, L., Liu, X., Zhou, L., Santosh, M., et al. (2012). Mesozoic  
768 basins in eastern China and their bearing on the deconstruction of the North  
769 China Craton. *Journal of Asian Earth Sciences*, 47, 64-79. <https://doi.org/10.1016/j.jseaes.2011.06.008>
- 771 Li, Y., Wu, Q., Pan, J., Zhang, F., & Yu, D. (2013), An upper-mantle S-wave velocity  
772 model for East Asia from Rayleigh wave tomography. *Earth and Planetary  
773 Science Letters*, 377-378, 367-377. <https://doi.org/10.1016/j.epsl.2013.06.033>
- 774 Liu, J., Han, J., & Fyfe, W. S. (2001). Cenozoic episodic volcanism and continental  
775 rifting in Northeast China and possible link to Japan Sea development as  
776 revealed from K-Ar geochronology. *Tectonophysics*, 339, 385-401.  
777 [https://doi.org/10.1016/S0040-1951\(01\)00132-9](https://doi.org/10.1016/S0040-1951(01)00132-9)
- 778 Liu, S., Wang, L., Gong, Y., Li, C., Li, H., & Han, Y. (2005). Thermal-rheological  
779 structure of the lithosphere beneath Jiyang Depression: Its implications for  
780 geodynamics. *Science in China Series D (Earth Sciences)*, 48, 1569-1584.  
781 <https://doi.org/10.1360/02YD0286>
- 782 Ma, J., Tian, Y., Liu, C., Zhao, D., Feng, X., & Zhu, H. (2018). P-wave tomography  
783 of Northeast Asia: Constraints on the western Pacific plate subduction and  
784 mantle dynamics. *Physics of the Earth and Planetary Interiors*, 274, 105-126.  
785 <https://doi.org/10.1016/j.pepi.2017.11.003>
- 786 Meng, Q. (2003). What drove late Mesozoic extension of the northern  
787 China-Mongolia tract? *Tectonophysics*, 369, 155-174.  
788 [https://doi.org/10.1016/S0040-1951\(03\)00195-1](https://doi.org/10.1016/S0040-1951(03)00195-1)
- 789 Menzies, M. A., & Xu, Y. (1998). Geodynamics of the North China Craton. In: Mantle  
790 Dynamics and Plate Interactions in East Asia. *American Geophysical Union  
791 Geodynamic Series*, 27, 155-165.
- 792 Minster, J. B., & Anderson, D. L. (1981). A model of dislocation controlled rheology  
793 for the mantle. *Philosophical Transactions of the Royal Society of London, Series  
794 A, Mathematical and Physical Sciences*, 299, 319–356.  
795 <https://doi.org/10.2307/36869>
- 796 Mishra, O. P., & Zhao, D. (2003). Crack density, saturation rate and porosity at the

- 797        2001 Bhuj, India, earthquake hypocenter: A fluid driven earthquake? *Earth and  
798        Planetary Science Letters*, 212, 393-405.  
799        [https://doi.org/10.1016/S0012-821X\(03\)00285-1](https://doi.org/10.1016/S0012-821X(03)00285-1)
- 800        Niu, Y. (2005). Generation and evolution of basaltic magmas: some basic concepts  
801        and a new view on the origin of Mesozoic-Cenozoic basaltic volcanism in  
802        Eastern China. *Geological Journal of China Universities*, 11, 9-46.
- 803        Paige, C., & Saunders, M. (1982). LSQR: an algorithm for sparse linear equations and  
804        sparse least squares. *ACM Transactions on Mathematical Software*, 8, 43–71.  
805        <https://doi.org/10.1145/355984.355989>
- 806        Pan, J., Li, Y., Wu, Q., & Yu, D. (2014). 3-D S-wave velocity structure of crust and  
807        upper-mantle beneath the northeast China. *Chinese Journal of Geophysics*, 57,  
808        2077-2087. <https://doi.org/10.6038/cjg20140705>
- 809        Pauselli, C., Ranalli, G., & Federico, C. (2010). Rheology of the Northern Apennines:  
810        lateral variations of lithospheric strength. *Tectonophysics*, 484, 27-35.  
811        <https://doi.org/10.1016/j.tecto.2009.08.029>
- 812        Qiu, N., Xu, W., Zuo, Y., Chang, J., & Liu, C. (2017). Evolution of Meso-Cenozoic  
813        thermal structure and thermal-rheological structure of the lithosphere in the  
814        Bohai Bay Basin, eastern North China Craton. *Earth Science Frontiers*, 24:  
815        13-26. <https://doi.org/10.13745/j.esf.2017.03.002>
- 816        Ranalli, G. (1994). Nonlinear flexure and equivalent mechanical thickness of the  
817        lithosphere. *Tectonophysics*, 240, 107–114.  
818        [https://doi.org/10.1016/0040-1951\(94\)90266-6](https://doi.org/10.1016/0040-1951(94)90266-6)
- 819        Ranalli, G. (2000). Rheology of the crust and its role in tectonic reactivation. *Journal  
820        of Geodynamics*, 30, 3-15. [https://doi.org/10.1016/S0264-3707\(99\)00024-1](https://doi.org/10.1016/S0264-3707(99)00024-1)
- 821        Ranalli, G., & Adams, M. (2013). Rheological contrast at the continental Moho:  
822        Effects of composition, temperature, deformation mechanism, and tectonic  
823        regime. *Tectonophysics*, 609, 480-490.  
824        <https://doi.org/10.1016/j.tecto.2012.10.037>
- 825        Ranalli, G., & Murphy, D. C. (1987). Rheological stratification of the lithosphere.  
826        *Tectonophysics*, 132, 281-295. [https://doi.org/10.1016/0040-1951\(87\)90348-9](https://doi.org/10.1016/0040-1951(87)90348-9)

- 827 Ren, J., Tamaki, K., Li, S., & Junxia, Z. (2002). Late Mesozoic and Cenozoic rifting  
828 and its dynamic setting in Eastern China and adjacent areas. *Tectonophysics*, 344,  
829 175-205. [https://doi.org/10.1016/S0040-1951\(01\)00271-2](https://doi.org/10.1016/S0040-1951(01)00271-2)
- 830 Rudnick, R., McDonough, W., & O'Connell, R. (1998). Thermal structure, thickness  
831 and composition of continental lithosphere. *Chemical Geology*, 145, 395–411.  
832 [https://doi.org/10.1016/S0009-2541\(97\)00151-4](https://doi.org/10.1016/S0009-2541(97)00151-4)
- 833 Rybach, L., & Buntebarth, G. (1984). The variation of heat generation, density and  
834 seismic velocity with rock type in the continental lithosphere. *Tectonophysics*,  
835 103, 335–344. [https://doi.org/10.1016/0040-1951\(84\)90095-7](https://doi.org/10.1016/0040-1951(84)90095-7)
- 836 Sengor, A. M. C., Natal'in, B. A., & Burtman, V. S. (1993). Evolution of the Altaiid  
837 tectonic collage and Palaeozoic crustal growth in Eurasia. *Nature*, 364, 299-307.  
838 <https://doi.org/10.1038/364299a0>
- 839 Shapiro, N. M., & Ritzwoller, M. H. (2004). Thermodynamic constraints on seismic  
840 inversions. *Geophysical Journal International*, 157, 1175-1188.  
841 <https://doi.org/10.1111/j.1365-246X.2004.02254.x>
- 842 Shen, W., Ritzwoller, M., Kang, D., Kim, Y., Lin, F., & Ning, J. (2016). A seismic  
843 reference model for the crust and uppermost mantle beneath China from surface  
844 wave dispersion. *Geophysical Journal International*, 206, 954-979.  
845 <https://doi.org/10.1093/gji/ggw175>
- 846 Sobolev, S. V., Zeyen, H., Stoll, G., Werling, F., Altherr, R., & Fuchs, K. (1996).  
847 Upper mantle temperatures from teleseismic tomography of French Massif  
848 Central including effects of composition, mineral reactions, anharmonicity,  
849 anelasticity and partial melt. *Earth and Planetary Science Letters*, 139, 147-163.  
850 [https://doi.org/10.1016/0012-821X\(95\)00238-8](https://doi.org/10.1016/0012-821X(95)00238-8)
- 851 Sun, Y., Dong, S., Zhang, H., Li, H., & Shi, Y. (2013). 3D thermal structure of the  
852 continental lithosphere beneath China and adjacent regions. *Journal of Asian  
853 Earth Sciences*, 62, 697-704. <https://doi.org/10.1016/j.jseaes.2012.11.020>
- 854 Tao, K., Liu, T., Ning, J., & Niu, F. (2014). Estimating sedimentary and crustal  
855 structure using wavefield continuation: theory, techniques and applications.  
856 *Geophysical Journal International*, 197, 443-457.

- 857 <https://doi.org/10.1093/gji/ggt515>
- 858 Tesauro, M., Kaban, M. K., & Cloetingh, S. (2012). Global strength and elastic  
859 thickness of the lithosphere. *Global and Planetary Change*, 90-91, 51-57.  
860 <https://doi.org/10.1016/j.gloplacha.2011.12.003>
- 861 Tesauro, M., Kaban, M. K., & Mooney, W. D. (2015). Variations of the lithospheric  
862 strength and elastic thickness in North America. *Geochemistry Geophysics  
863 Geosystems*, 16, 2197-2220. <https://doi.org/10.1002/2015GC005937>
- 864 Tian, Y., Zhao, D., Sun, R., & Teng, J. (2009). Seismic imaging of the crust and upper  
865 mantle beneath the North China Craton. *Physics of the Earth and Planetary  
866 Interiors*, 172, 169-182. <https://doi.org/10.1016/j.pepi.2008.09.002>
- 867 Tian, Y., Legendre, C. P., Zhou, T., Han, J., Wu, M., Zhao, L., et al. (2017). High  
868 resolution anisotropic phase velocity tomography of Northeast China and its  
869 implication. *Chinese Journal of Geophysics*, 60, 1659-1675.  
870 <https://doi.org/10.6038/cjg20170505>
- 871 Tian, Y., Ma, J., Liu, C., Feng, X., Liu, T., Zhu, H., et al. (2019). Effects of subduction  
872 of the western Pacific plate on tectonic evolution of Northeast China and  
873 geodynamic Implications. *Chinese Journal of Geophysics*, 62, 1071-1082.  
874 <https://doi.org/10.6038/cjg2019M0061>
- 875 Tian, Y., Zhu, H., Zhao, D., Liu, C., Feng, X., Liu, T., et al. (2016). Mantle transition  
876 zone structure beneath the Changbai volcano: Insight into deep slab dehydration  
877 and hot upwelling near the 410 km discontinuity. *Journal of Geophysical  
878 Research: Solid Earth*, 121, 5794-5808. <https://doi.org/10.1002/2016JB012959>
- 879 Tian, Z., Han, P., & Xu, K. (1992). The Mesozoic-Cenozoic East China rift system.  
880 *Tectonophysics*, 208, 341-363. [https://doi.org/10.1016/0040-1951\(92\)90354-9](https://doi.org/10.1016/0040-1951(92)90354-9)
- 881 Vacher, P., Mocquet, A., & Sotin, C. (1998). Computation of seismic profiles from  
882 mineral physics: the importance of non-olivine components for explaining the  
883 660 depth discontinuity. *Physics of the Earth and Planetary Interiors*, 106,  
884 275-298. [https://doi.org/10.1016/S0031-9201\(98\)00076-4](https://doi.org/10.1016/S0031-9201(98)00076-4)
- 885 Wang, F., Zhou, X., Zhang, L., Ying, J., Zhang, Y., Wu, F., et al. (2006). Late  
886 Mesozoic volcanism in the Great Xing'an Range (NE China): Timing and

- 887 implications for the dynamic setting of NE Asia. *Earth and Planetary Science*  
888 *Letters*, 251, 179-198. <https://doi.org/10.1016/j.epsl.2006.09.007>
- 889 Wang, J., & Li, C. (2018). Curie point depths in Northeast China and their geothermal  
890 implications for the Songliao Basin. *Journal of Asian Earth Sciences*, 163,  
891 177-193. <https://doi.org/10.1016/j.jseaes.2018.05.026>
- 892 Wang, Y. (2001). Heat flow pattern and lateral variations of lithosphere strength in  
893 China mainland: constraints on active deformation. *Physics of the Earth and*  
894 *Planetary Interiors*, 126, 121-146.  
895 [https://doi.org/10.1016/S0031-9201\(01\)00251-5](https://doi.org/10.1016/S0031-9201(01)00251-5)
- 896 Wang, Y., & Cheng, S. (2011). Thermal state and rheological strength of the  
897 lithosphere beneath the Eastern China. *Geotectonica et Metallogenica*, 35, 12-23.
- 898 Wang, Y., & Wang, J. (1992). Using seismic velocity data to calculate the deep crustal  
899 rock heat production-along the Shicheng-Huian profile. *Chinese Science Bulletin*,  
900 7, 633–636.
- 901 Watt, J. P., Davies, G. F., & O'Connell R. J. (1976). The elastic properties of  
902 composite materials. *Reviews of Geophysics*, 14, 541-563.  
903 <https://doi.org/10.1029/RG014i004p00541>
- 904 Weertman, J. (1970). The creep strength of the Earth's mantle. *Reviews of Geophysics*,  
905 8, 145-168. <https://doi.org/10.1029/RG008i001p00145>
- 906 Wei, W., Hammond, J., Zhao, D., Xu, J., Liu, Q., Gu, Y., et al. (2019). Seismic  
907 evidence for a mantle transition zone origin of the Wudalianchi and Halaha  
908 volcanoes in northeast China. *Geochemistry, Geophysics, Geosystems*, 20,  
909 398-416. <https://doi.org/10.1029/2018GC007663>
- 910 Wei, W., Zhao, D., & Xu, J. (2013). P-wave anisotropic tomography in Southeast  
911 Tibet: New insight into the lower crustal flow and seismotectonics. *Physics of the*  
912 *Earth and Planetary Interiors*, 222, 47-57.  
913 <https://doi.org/10.1016/j.pepi.2013.07.002>
- 914 Wessel, P., & Smith, W. (1998). New, improved version of generic mapping tools  
915 released. *Eos Transactions, American Geophysical Union*, 79, 579.  
916 <https://doi.org/10.1029/98EO00426>

- 917 Wu, F., Ye, M., & Zhang, S. (1995). Geodynamic model of the Manzhouli-Suifenhe  
918 geoscience transect. *Earth Science-Journal of China University of Geosciences*,  
919 20, 535-539.
- 920 Xia, S., Zhou, P., Zhao, D., & Cao, J. (2020). Seismogenic structure in the source  
921 zone of the 1918 M7.5 NanAo earthquake in the northern South China Sea.  
922 *Physics of the Earth Planetary Interiors*, 302, 106472.  
923 <https://doi.org/10.1016/j.pepi.2020.106472>
- 924 Xu, M., Li, Y., Hou, H., Wang, C., Gao, R., Wang, H., et al. (2017). Structural  
925 characteristics of the Yilan-Yitong and Dunhua-Mishan faults as northern  
926 extensions of the Tancheng-Lujiang Fault Zone: New deep seismic reflection  
927 results. *Tectonophysics*, 706-707, 35-45.  
928 <https://doi.org/10.1016/j.tecto.2017.03.018>
- 929 Xu, P., & Zhao, D. (2009). Upper-mantle velocity structure beneath the North China  
930 Craton: Implications for lithospheric thinning. *Geophysical Journal International*,  
931 177, 1279-1283. <https://doi.org/10.1111/j.1365-246X.2009.04120.x>
- 932 Xu, W., Pei, F., Wang, F., Meng, E., Ji, W., Yang, D., et al. (2013). Spatial-temporal  
933 relationships of Mesozoic volcanic rocks in NE China: Constraints on tectonic  
934 overprinting and transformations between multiple tectonic regimes. *Journal of  
935 Asian Earth Sciences*, 74, 167-193. <https://doi.org/10.1016/j.jseaes.2013.04.003>
- 936 Xu, Y. (2007). Diachronous lithospheric thinning of the North China Craton and  
937 formation of the Daxin'anling-Taihangshan gravity lineament. *Lithos*, 96,  
938 281-298. <https://doi.org/10.1016/j.lithos.2006.09.013>
- 939 Yan, D., Tian, Y., Zhao, D., Liu, C., Zhu, H., & Li, H. (2019). Upper mantle  
940 temperature structure of the North China Craton. *Physics of the Earth and  
941 Planetary Interiors*, 293, 106269. <https://doi.org/10.1016/j.pepi.2019.106269>
- 942 Yang, B., Liu, W., Wang, X., Li, Q., Wang, J., Zhao, X., et al. (2005). Geophysical  
943 characteristics of Daxinganling gravitational gradient zone in the East China and  
944 its geodynamic mechanism. *Chinese Journal of Geophysics*, 48, 86-97.  
945 <https://doi.org/10.1002/cjg2.631>
- 946 Yang, S., Xiong, X., Zheng, Y., & Shan, B. (2013). Upper-mantle temperature and

- 947 lithospheric thickness of North China. *Chinese Journal of Geophysics*, 56,  
948 3855-3867. <https://doi.org/10.6038/cjg20131127>
- 949 Zang, S., Li, C., & Wei, R. (2002b). The determination of rheological mechanics of  
950 lithosphere and the influencing factors on the rheological strength of lithosphere.  
951 *Progress in Geophysics*, 17, 50-60.
- 952 Zang, S., Liu, Y., & Ning, J. (2002a). Thermal structure of the lithosphere in North  
953 China. *Chinese Journal of Geophysics*, 45, 51-62.  
954 <https://doi.org/10.1002/cjg2.216>
- 955 Zang, S., Wei, R., & Liu, Y. (2005). Three-dimensional rheological structure of the  
956 lithosphere in the Ordos and its adjacent area. *Geophysical Journal International*,  
957 163, 339-356.
- 958 Zang, S., Wei, R., & Ning, J. (2007). Effect of brittle fracture on the rheological  
959 structure of the lithosphere and its application in the Ordos. *Tectonophysics*, 429,  
960 267-285. <https://doi.org/10.1016/j.tecto.2006.10.006>
- 961 Zhang, B., Lei, J., Yuan, X., Zhang, G., He, J., & Xu, Q. (2020). Detailed Moho  
962 variations under Northeast China inferred from receiver function analyses and  
963 their tectonic implications. *Physics of the Earth and Planetary Interiors*, 300,  
964 106448. <https://doi.org/10.1016/j.pepi.2020.106448>
- 965 Zhang, L., & Tang, X. (1983). The underthrusting movement of the western pacific  
966 plate and the deep focus earthquake zone of Northeast China. *Chinese Journal of  
967 Geophysics*, 26, 331-340.
- 968 Zhang, L., Liu, Q., & He, L. (2016). The different lithospheric thermal structure of  
969 North China Craton and its implications. *Chinese Journal of Geophysics*, 59,  
970 3618-3626. <https://doi.org/10.6038/cjg20161009>
- 971 Zhang, R., Wu, Q., Sun, L., He, J., & Gao, Z. (2014). Crustal and lithospheric  
972 structure of Northeast China from S-wave receiver functions. *Earth and  
973 Planetary Science Letters*, 401, 196-205.  
974 <https://doi.org/10.1016/j.epsl.2014.06.017>
- 975 Zhao, D., & Tian, Y. (2013). Changbai intraplate volcanism and deep earthquakes in  
976 East Asia: a possible link? *Geophysical Journal International*, 195, 706-724.

- 977           <https://doi.org/10.1093/gji/ggt289>
- 978   Zhao, D., Hasegawa, A., & Horiuchi, S. (1992). Tomographic imaging of P and S  
979       wave velocity structure beneath northeastern Japan. *Journal of Geophysical*  
980       *Research*, 97, 19909-19928. <https://doi.org/10.1029/92JB00603>
- 981   Zhao, D., Hasegawa, A., & Kanamori, H. (1994). Deep structure of Japan subduction  
982       zone as derived from local, regional, and teleseismic events. *Journal of*  
983       *Geophysical Research*, 99, 22313-22329. <https://doi.org/10.1029/94JB01149>
- 984   Zhao, D., Lei, J., & Tang, Y. (2004). Origin of the Changbai volcano in northeast  
985       China: Evidence from seismic tomography. *Chinese Science Bulletin*, 49,  
986       1401-1408. <https://doi.org/10.1360/04wd0125>
- 987   Zhao, D., Tian, Y., Lei, J., Liu, L., & Zheng, S. (2009). Seismic image and origin of  
988       the Changbai intraplate volcano in East Asia: Role of big mantle wedge above  
989       the stagnant Pacific slab. *Physics of the Earth and Planetary Interiors*, 173,  
990       197-206. <https://doi.org/10.1016/j.pepi.2008.11.009>
- 991   Zhou, J., & Wilde, S. A. (2013). The crustal accretion history and tectonic evolution  
992       of the NE China segment of the Central Asian Orogenic Belt. *Gondwana*  
993       *Research*, 23, 1365-1377. <https://doi.org/10.1016/j.gr.2012.05.012>
- 994   Zhu, R., Chen, L., Wu, F., & Liu, J. (2011). Timing, scale and mechanism of the  
995       destruction of the North China Craton. *Science China (Earth Sciences)*, 54,  
996       789-797. <https://doi.org/10.1007/s11430-011-4203-4>
- 997

998 **Figure captions:**

999 **Figure 1.** Surface topography and tectonic settings of Northeast China. The white  
1000 solid line shows the location of the North-South Gravity Lineament (NSGL). The white  
1001 dashed lines depict boundaries of major tectonic blocks. The red triangles  
1002 denote major active volcanoes. The east-west dashed lines denote locations of eight  
1003 vertical cross-sections shown in Figure 3 and Figure 4. ABGV: Abaga Volcano;  
1004 HLHV: Halaha Volcano; WDLCV: Wudalianchi Volcano; JPHV: Jingpohu Volcano;  
1005 LGV: Longgang Volcano; CBV: Changbai Volcano.

1006

1007 **Figure 2.** Map views of the 3-D temperature structure estimated from a joint  
1008 inversion of Vp and Vs models. The layer depth is shown at the upper-left corner of  
1009 each map. The red and blue colors represent high and low temperatures, respectively.  
1010 The temperature scale is shown below each panel. Other labels are the same as those  
1011 in Figure 1.

1012

1013 **Figure 3.** (a-h) East-west vertical cross-sections of the 3-D lithospheric temperature  
1014 distribution along the eight profiles shown in Figure 1. The black arrow above each  
1015 panel indicates the location of NSGL, and the red triangles denote major active  
1016 volcanoes. The black dashed line in each panel depicts the estimated lower boundary  
1017 of the thermal lithosphere.

1018

1019 **Figure 4.** The same as Figure 3 but for the 3-D lithospheric temperature distribution  
1020 obtained by solving the 1-D steady-state heat conduction equation. The black dashed  
1021 line in each panel depicts the Moho discontinuity.

1022

1023 **Figure 5.** Distribution of the thermal lithosphere thickness in NE China.

1024

1025 **Figure 6.** Distribution of the integrated lithospheric strength beneath NE China. The  
1026 white circles denote epicenters of crustal earthquakes ( $M_b \geq 4.0$ ) occurring during  
1027 1970 to 2020, which are listed in the ISC catalog.

1028

1029 **Figure 7.** (a-d) East-west vertical cross-sections of the lithospheric strength along  
1030 four profiles. The black dashed line in each panel depicts the Moho discontinuity. The  
1031 white circles in each panel denote crustal earthquakes ( $M_b \geq 4.0$ ) during 1970 to 2020,  
1032 which are located within a 50-km width of each profile.

1033

1034 **Figure 8.** Yield strength envelopes in six key areas of NE China. The dashed lines h1  
1035 and h2 in each panel denote the bottom of the upper crust and the middle crust,  
1036 respectively. BR(a) represents the brittle part where the frictional sliding mechanism  
1037 is dominant. BR(b) means that the dominant deformation mechanism is brittle fracture.  
1038 DR represents the ductile part.

1039

1040 **Figure 9.** Relationship between temperature and P- and S-wave velocities computed  
1041 for the lithosphere at 50 km depth. The black and blue lines show the results for  
1042 on-cratonic and off-cratonic mantle models, respectively, with the same anelastic  
1043 correction. The red lines show the results for the on-cratonic mantle model with a  
1044 reduced anelastic correction.

1045

1046 **Figure 10.** A cartoon showing the structure and dynamics of the lithosphere and upper  
1047 mantle beneath NE China as well as the formation mechanism of Cenozoic intraplate  
1048 volcanoes (red triangles). The red and purple dots denote crustal earthquakes and  
1049 deep-focus earthquakes, respectively.

1050

**Figure 1.**

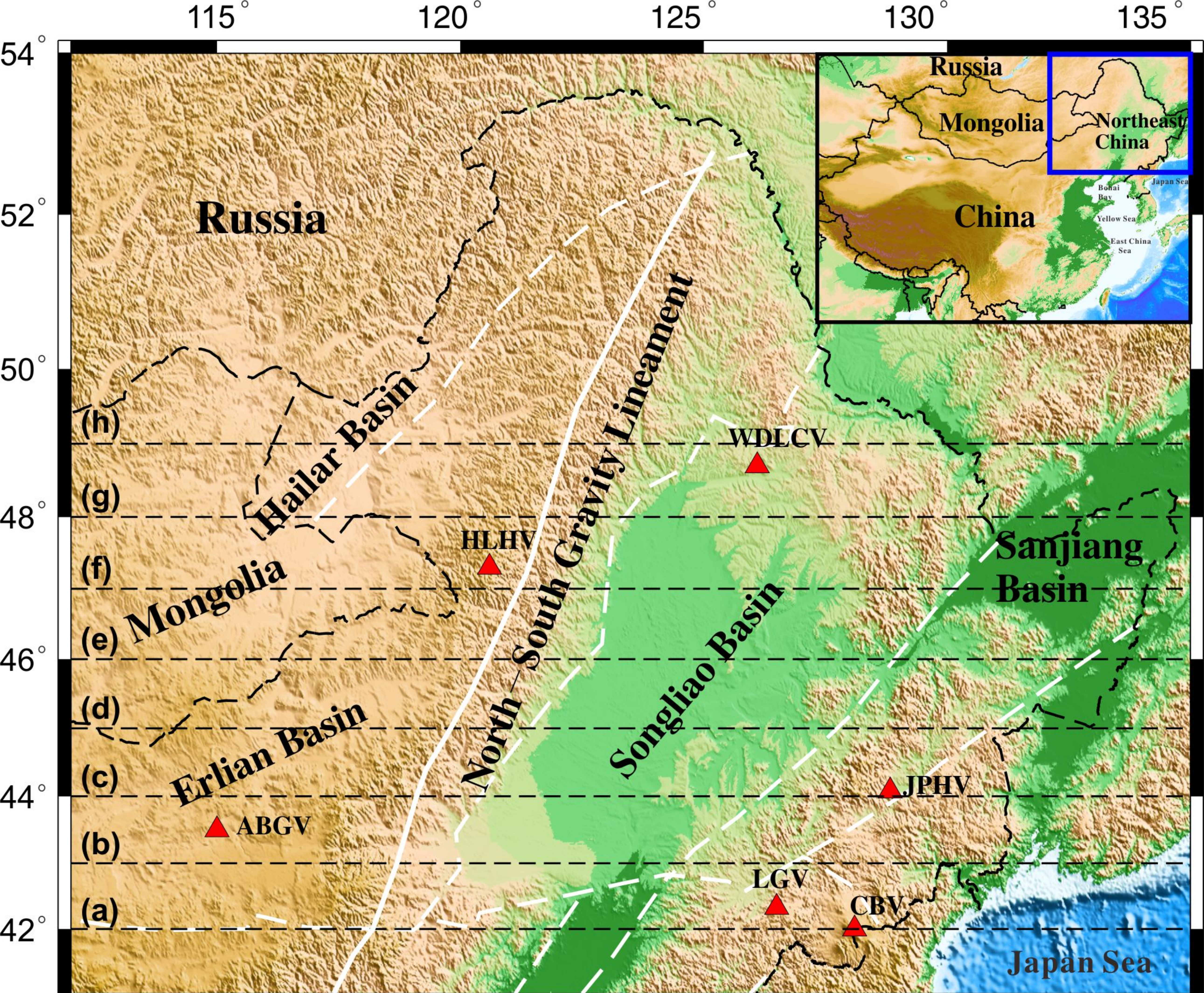


**Figure 2.**

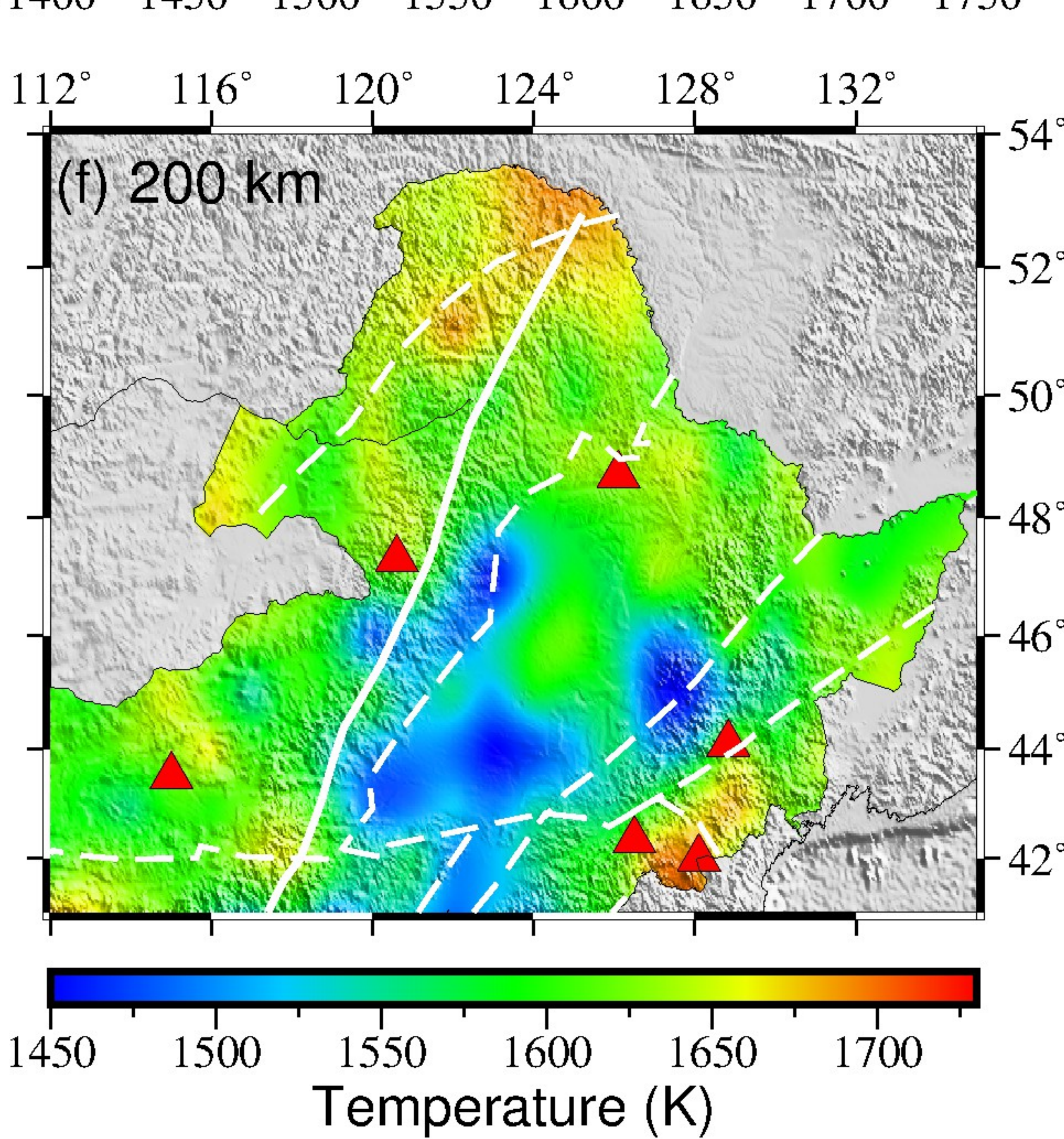
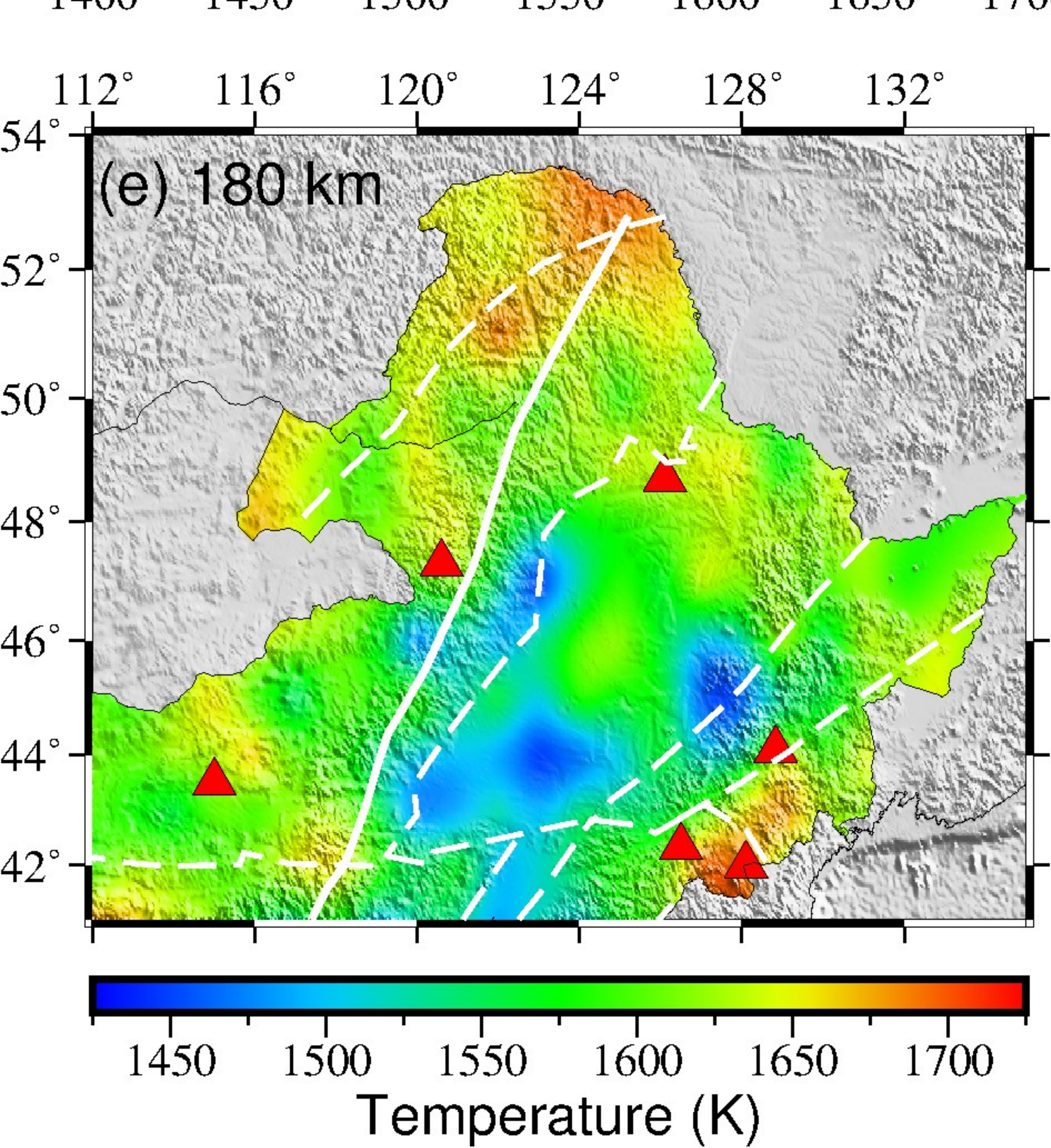
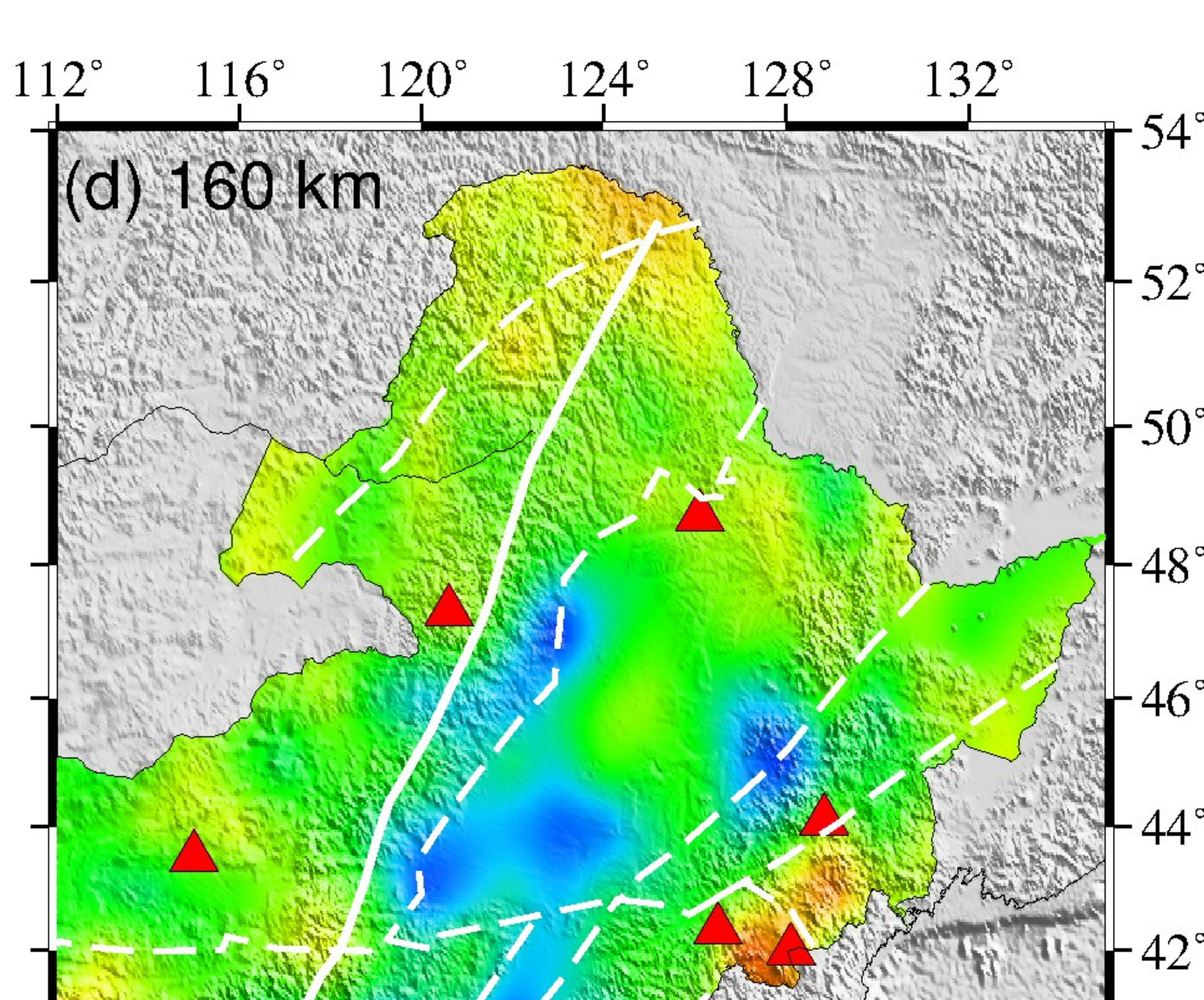
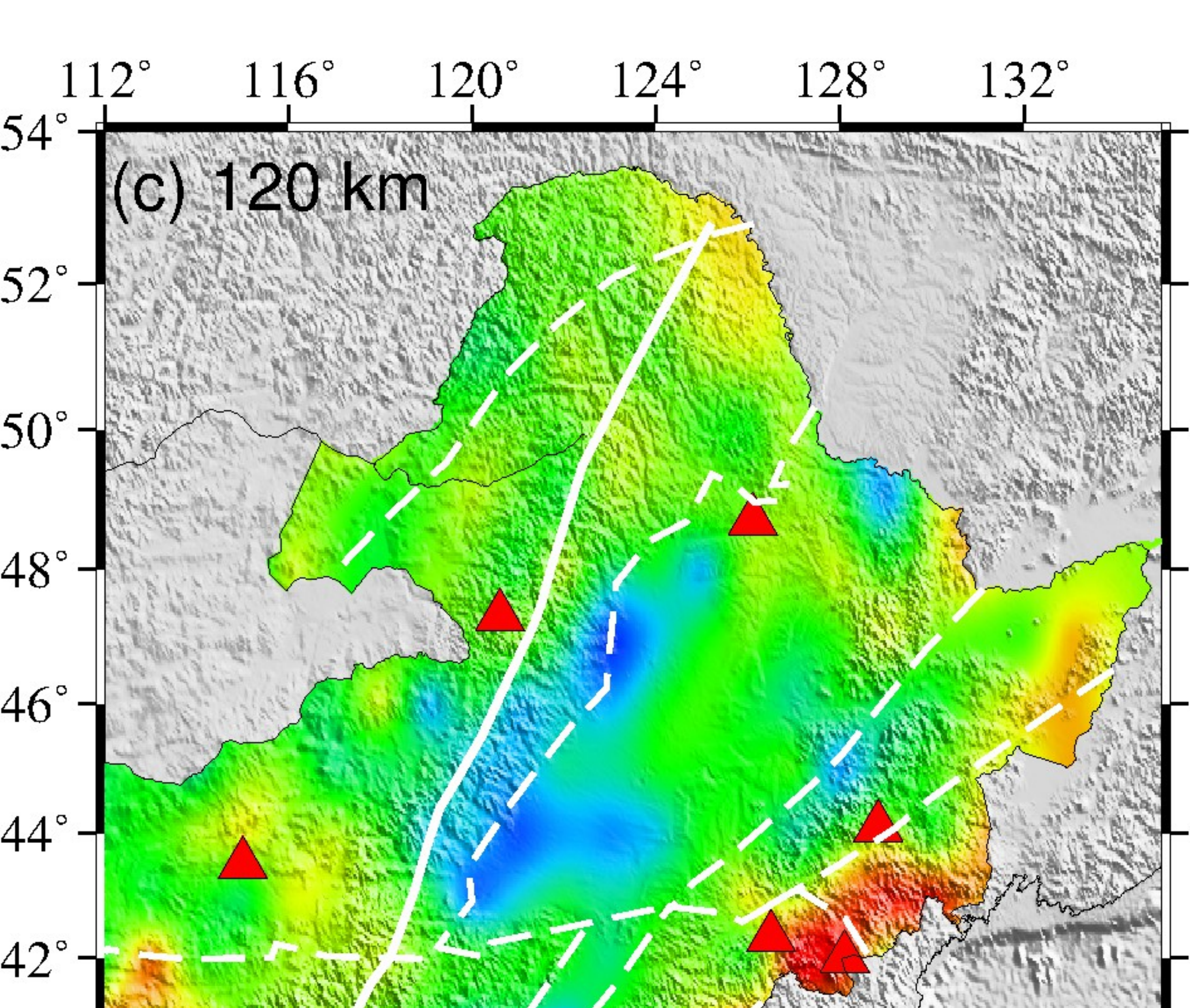
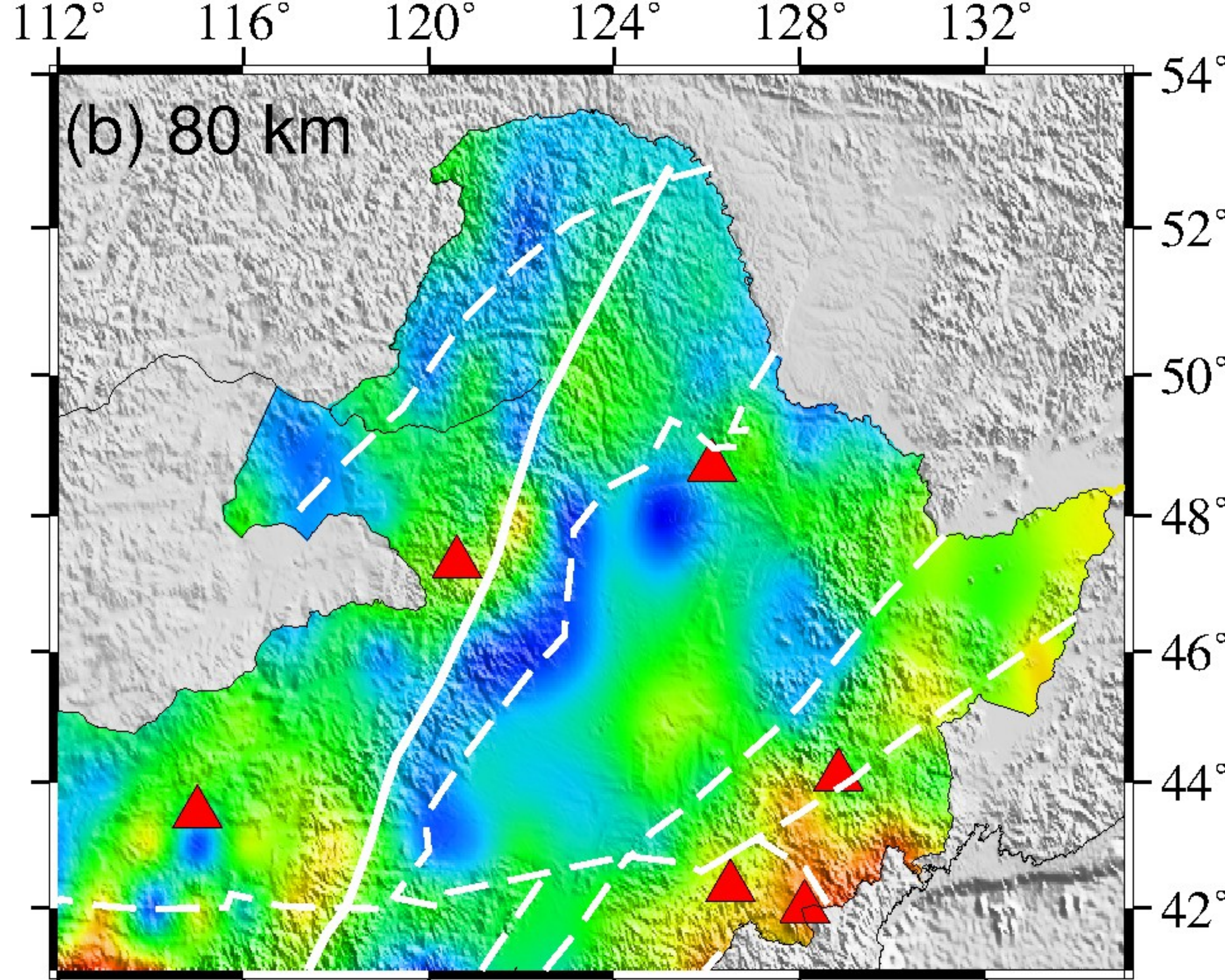
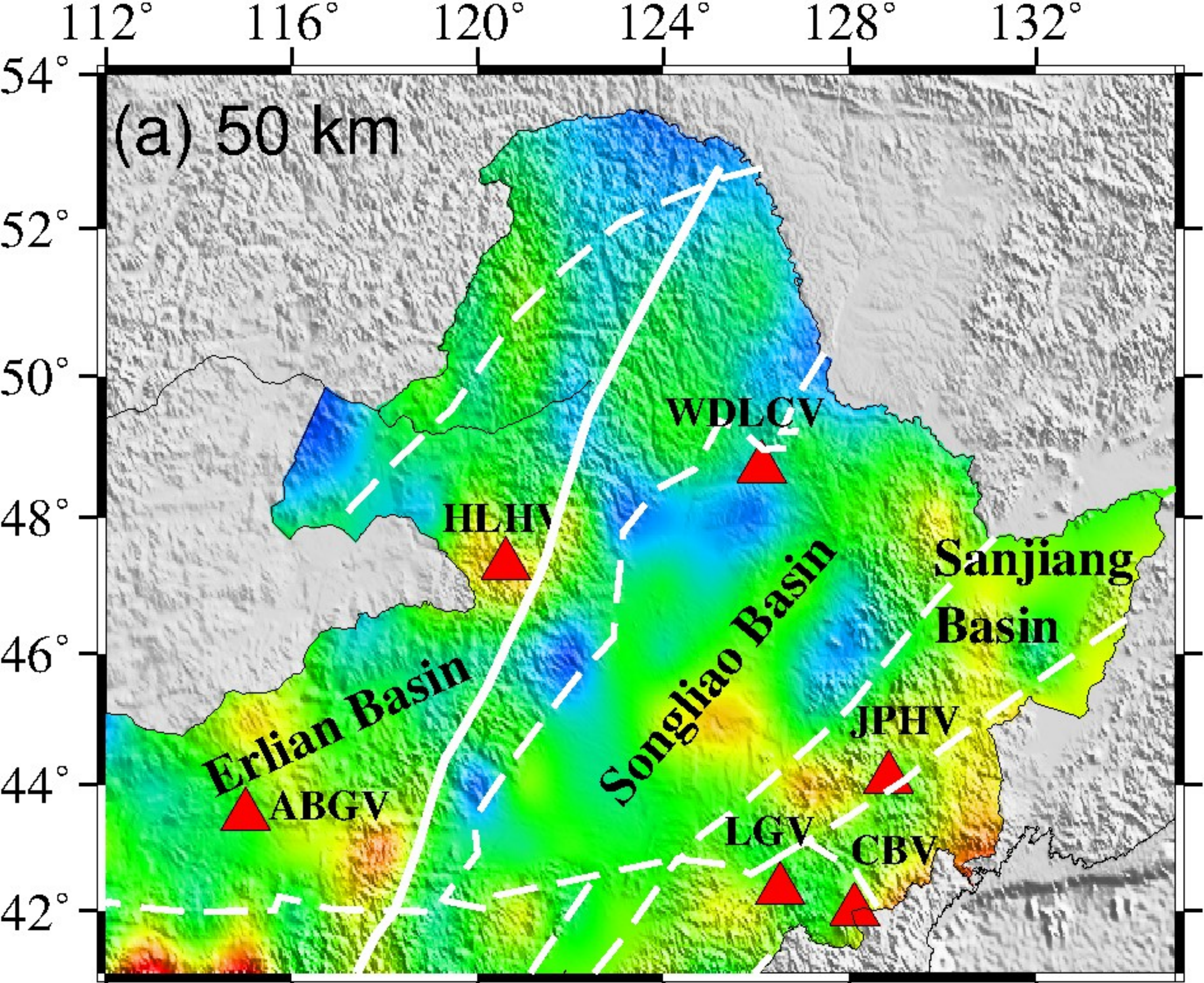


**Figure 3.**

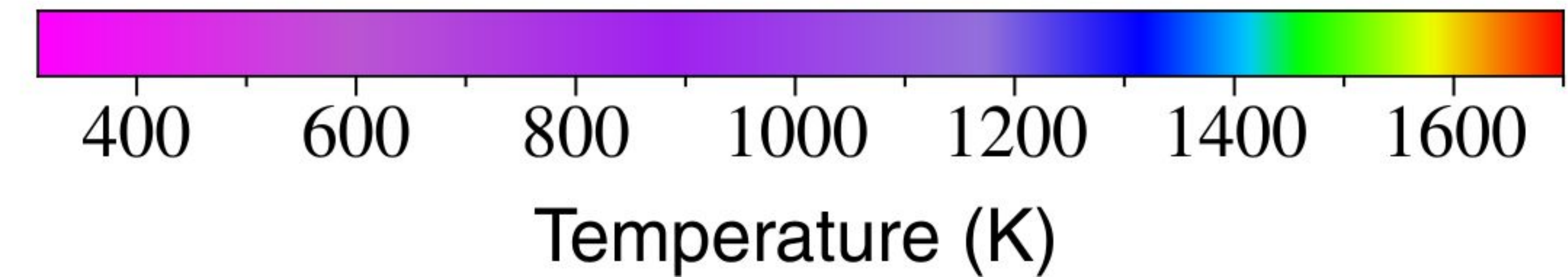
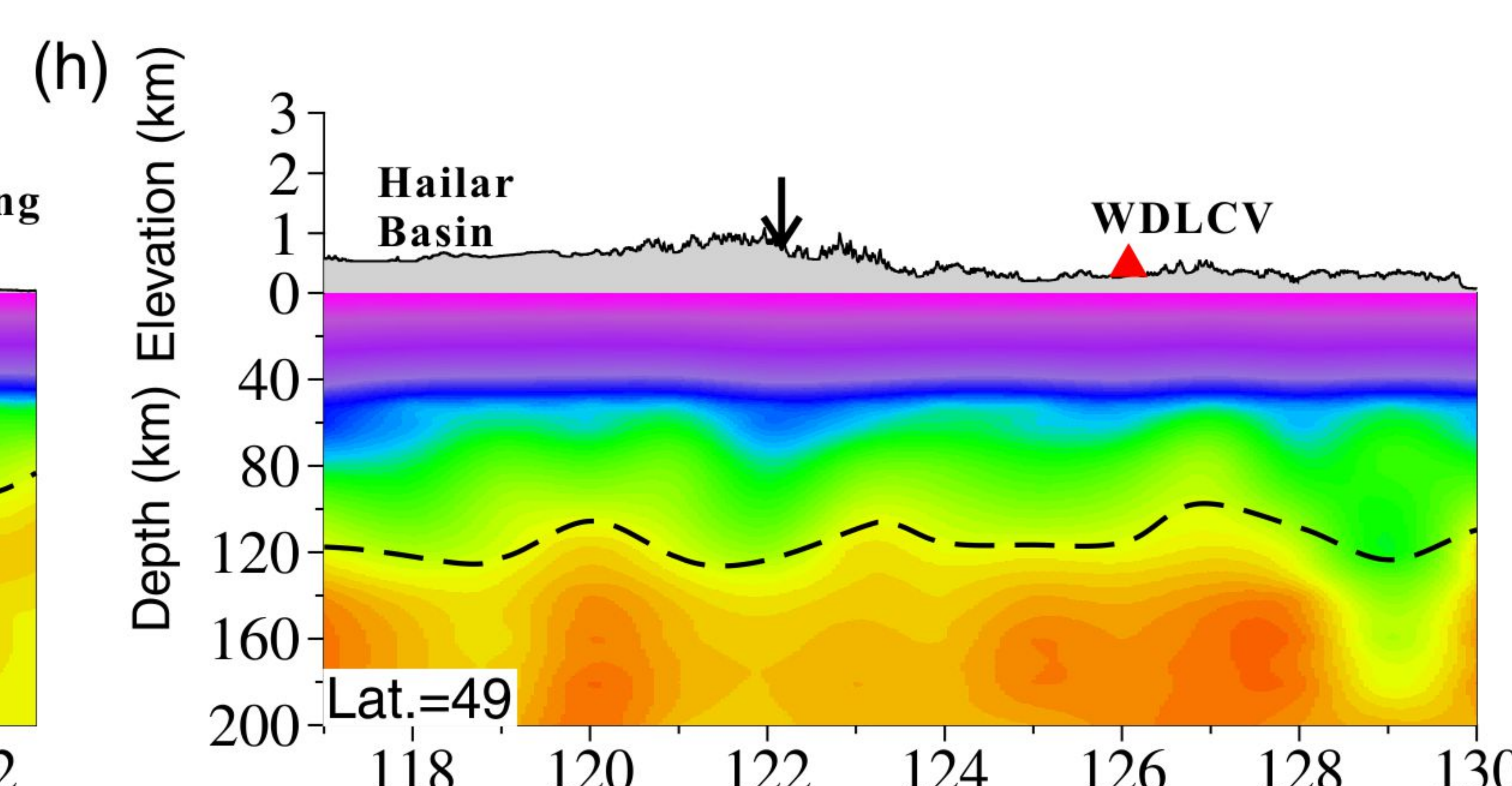
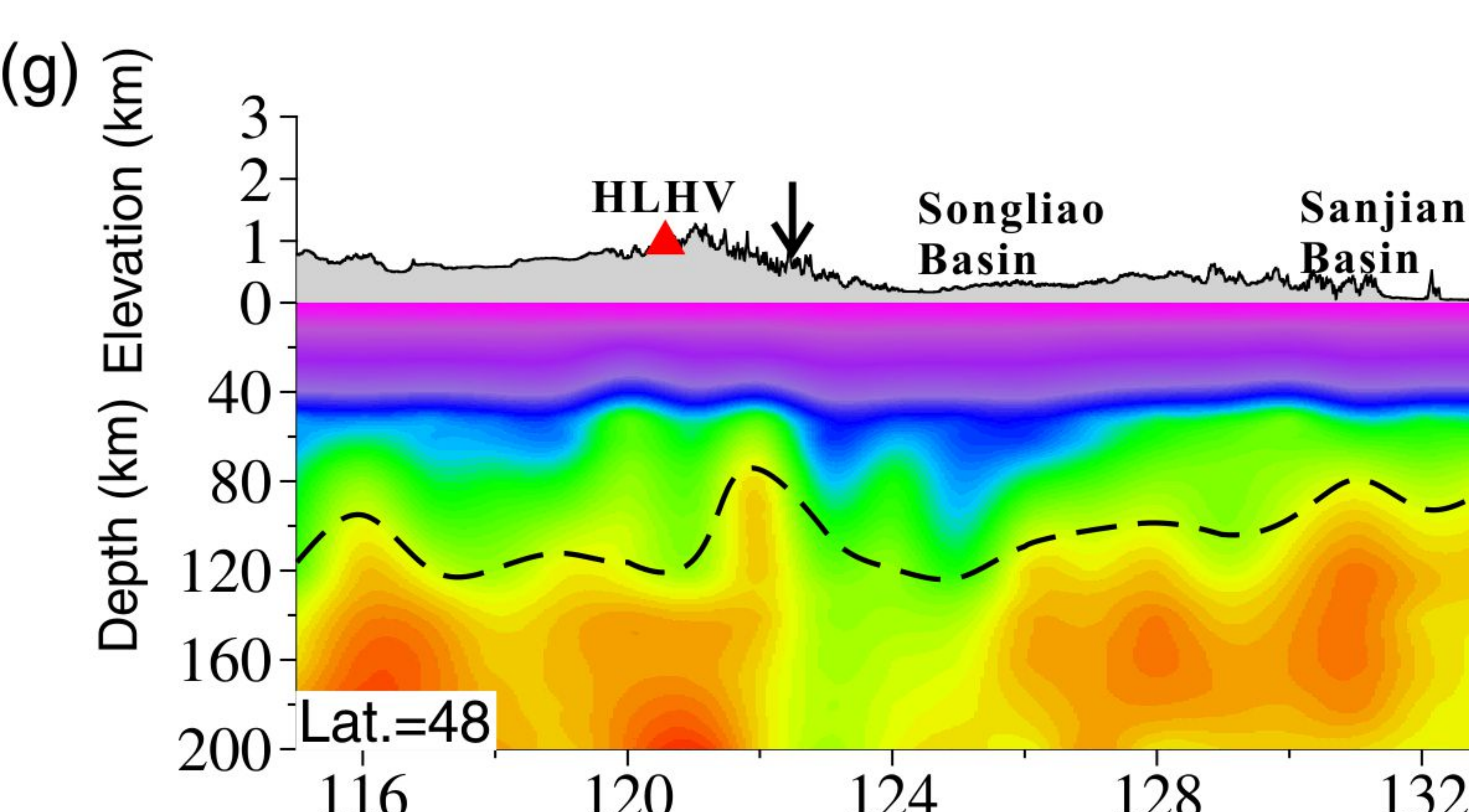
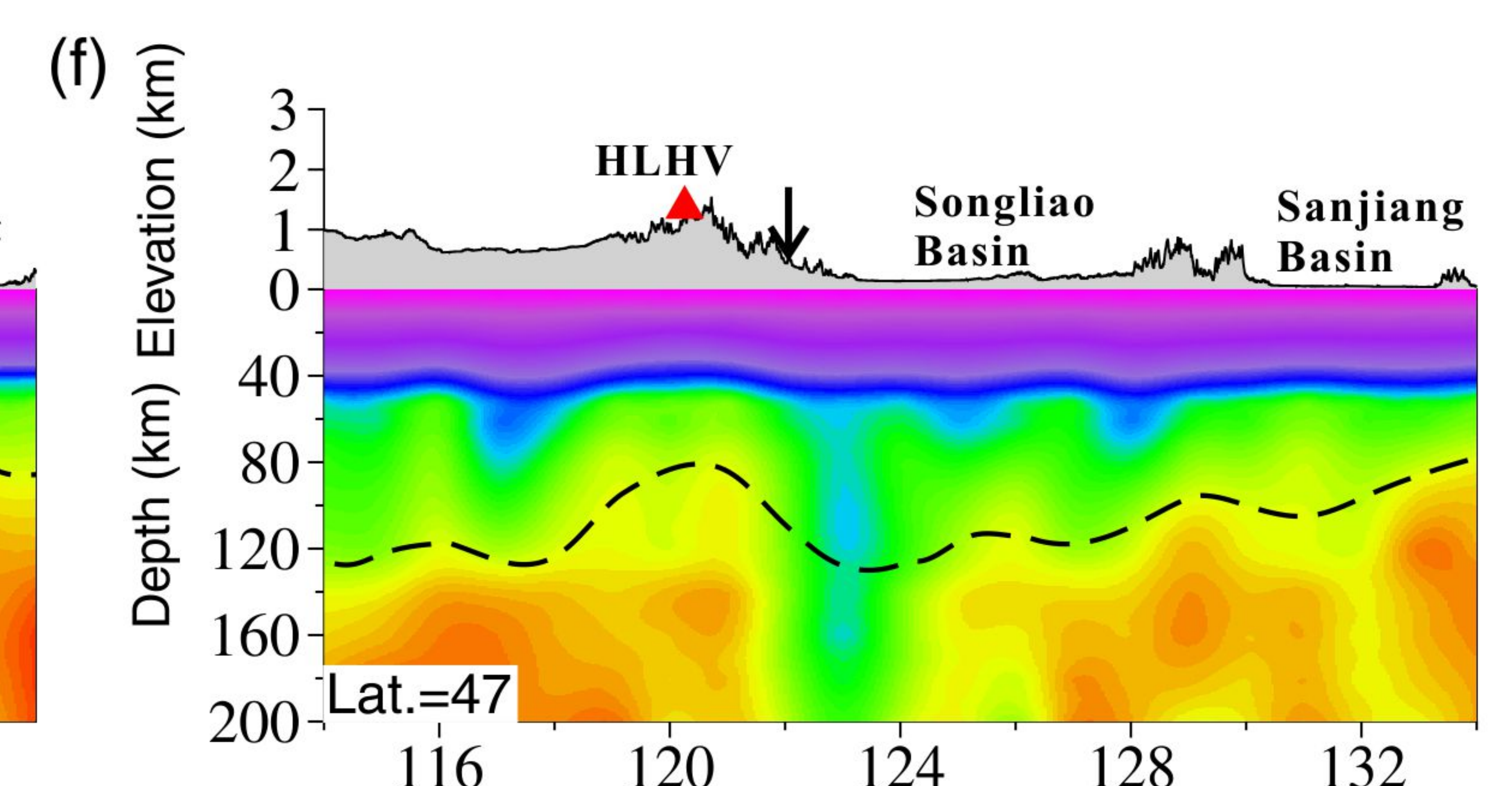
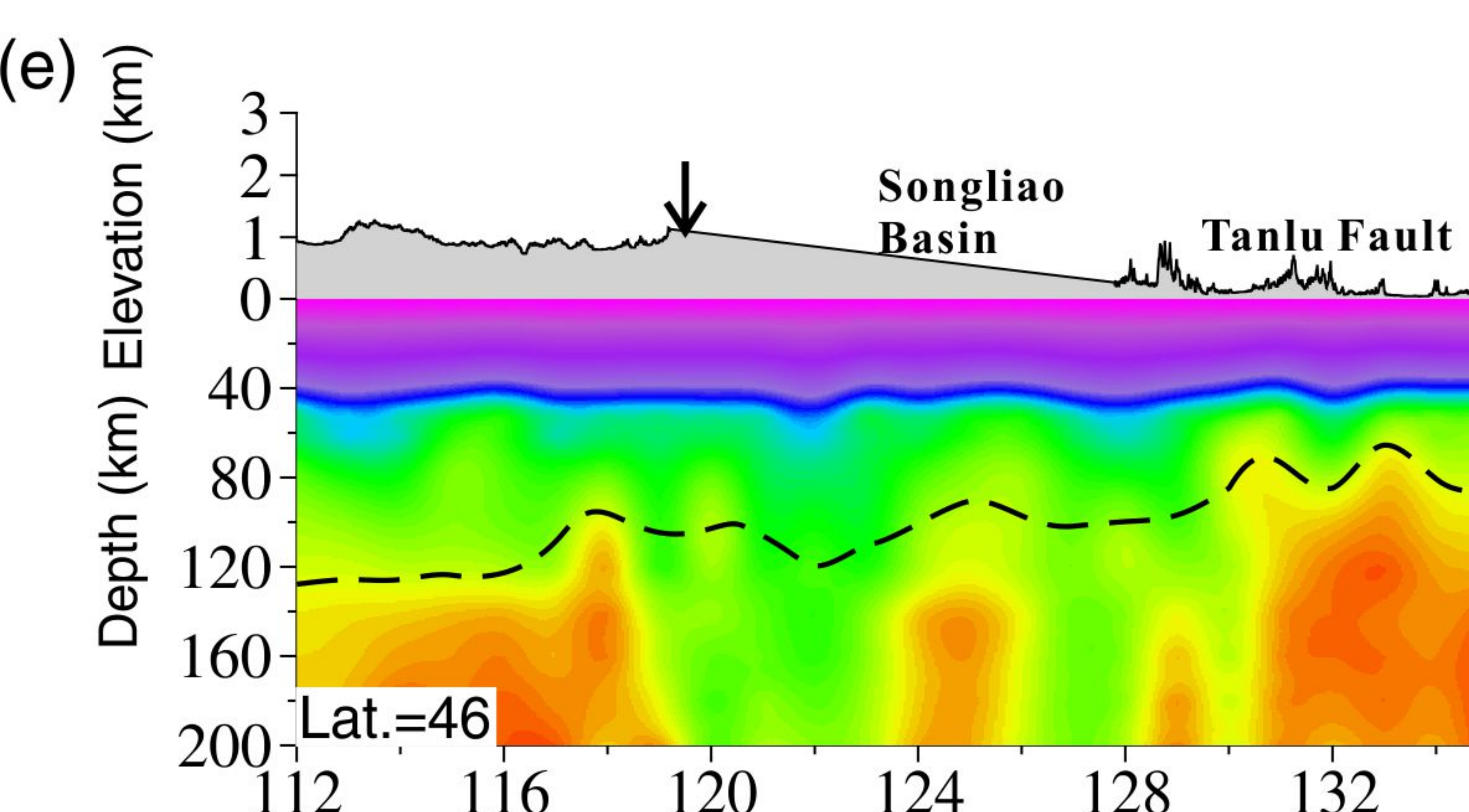
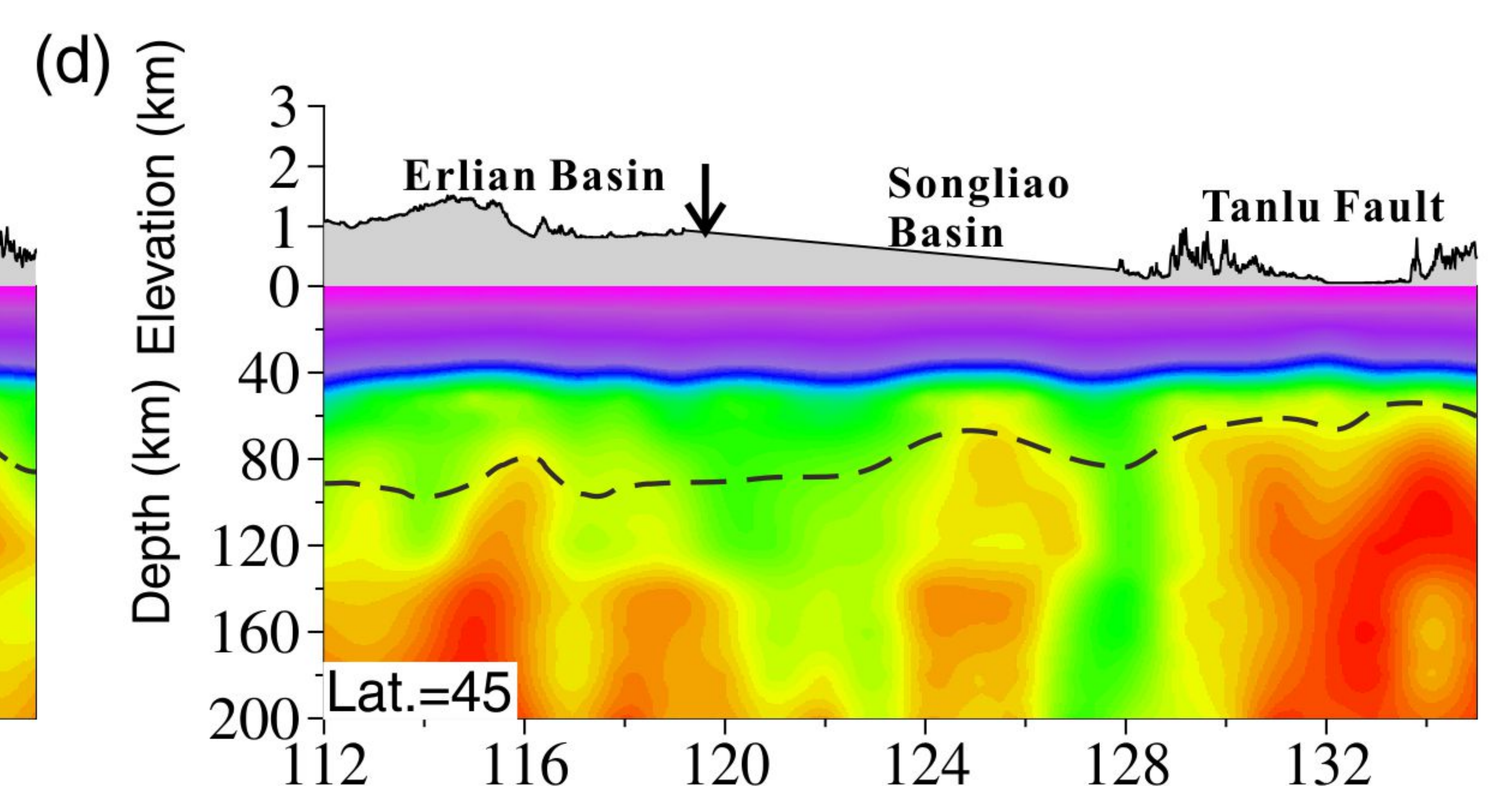
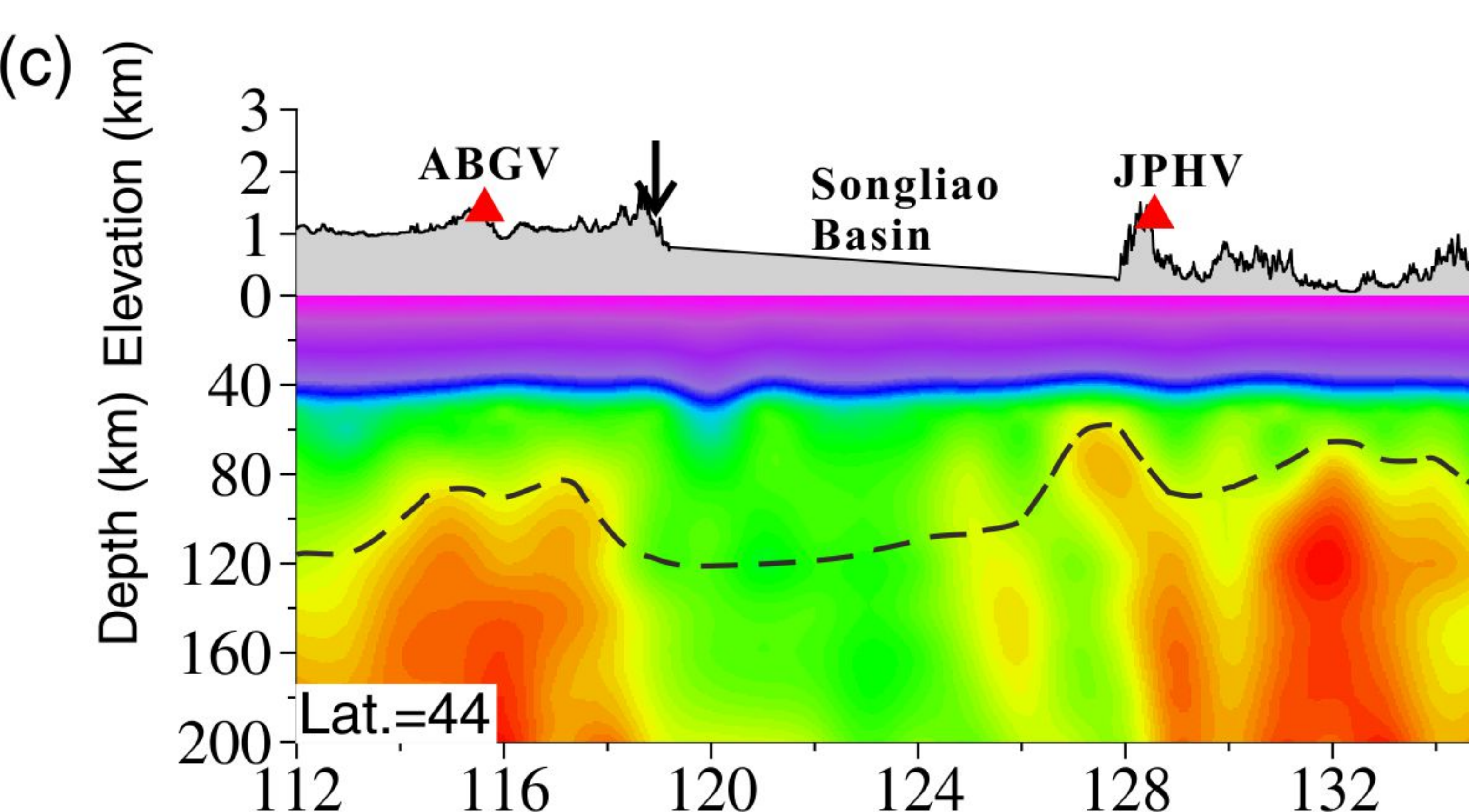
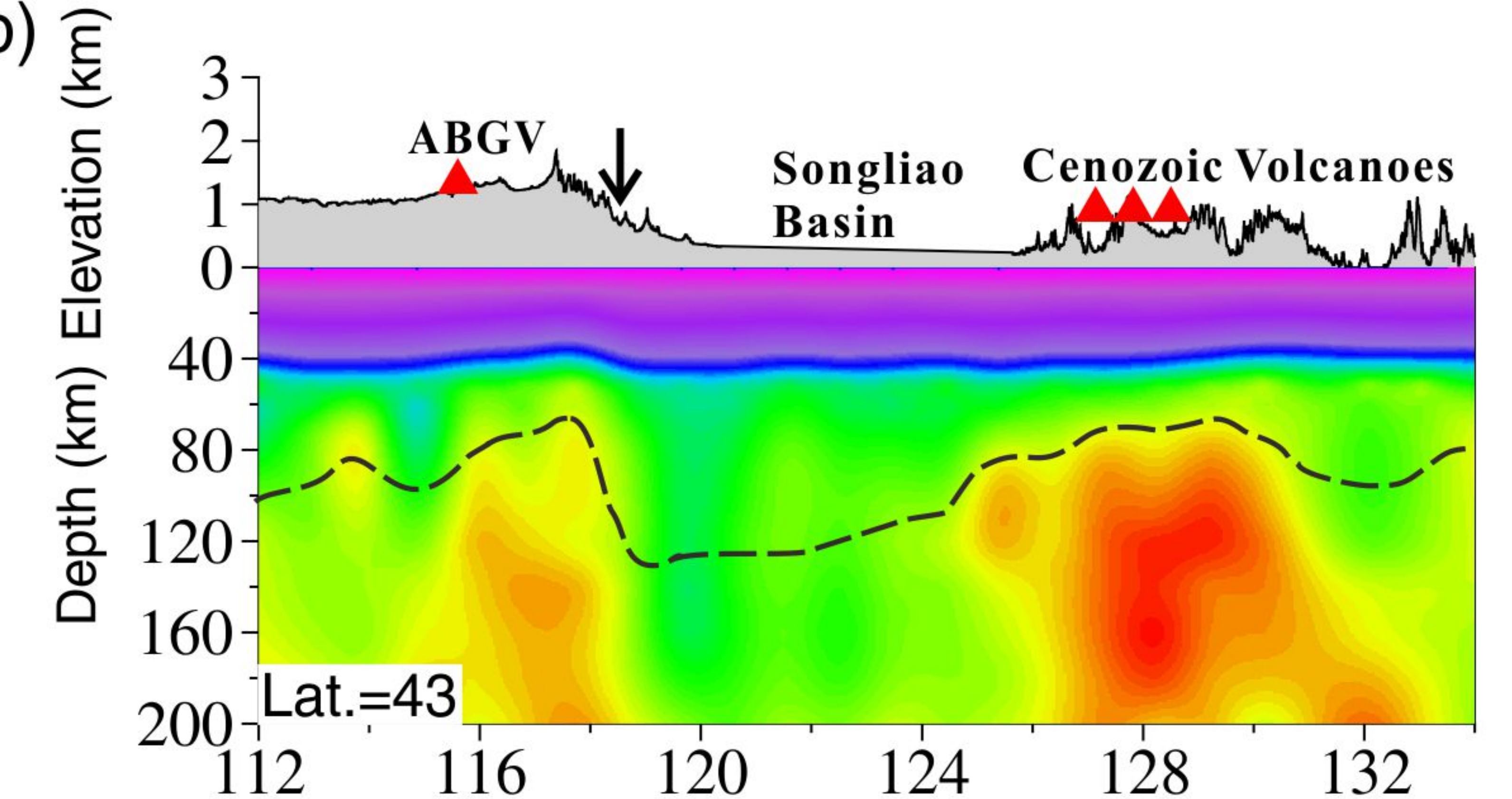
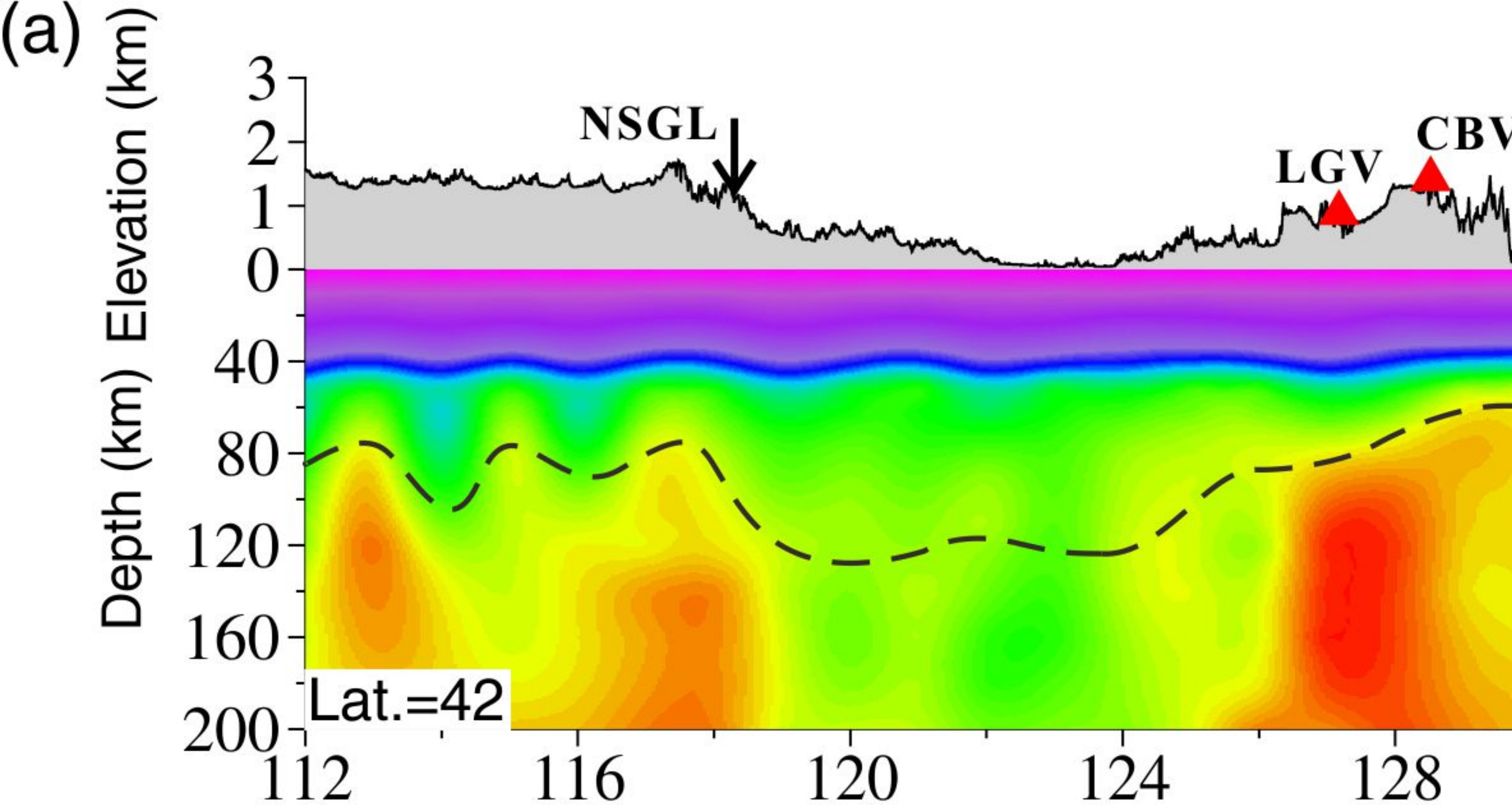


**Figure 4.**

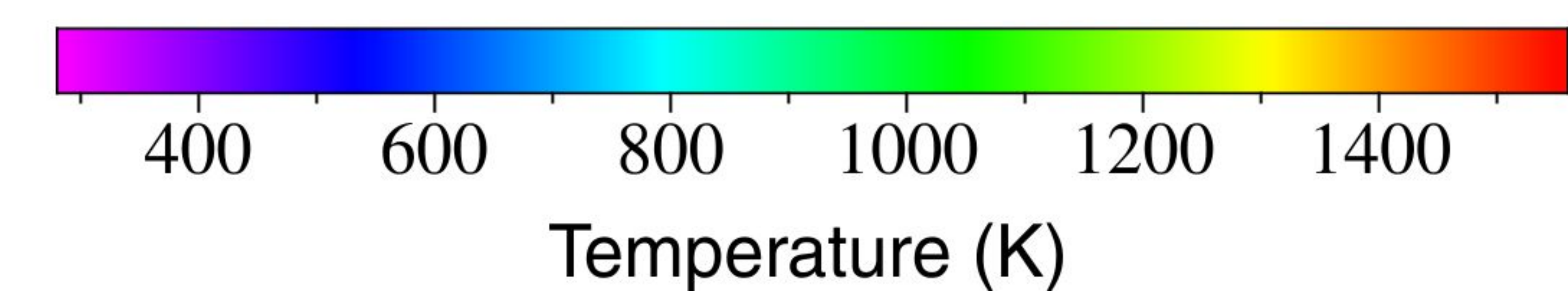
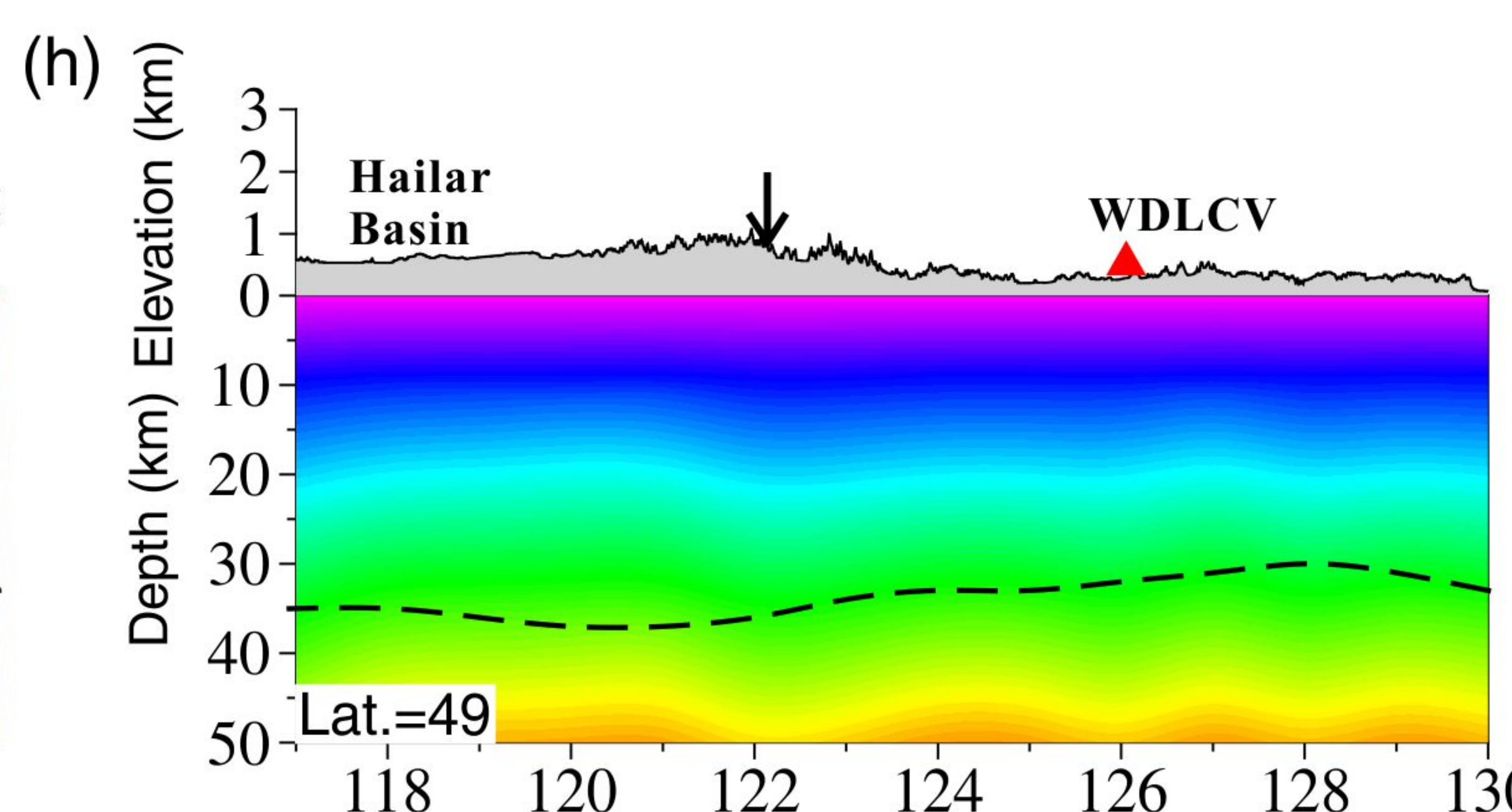
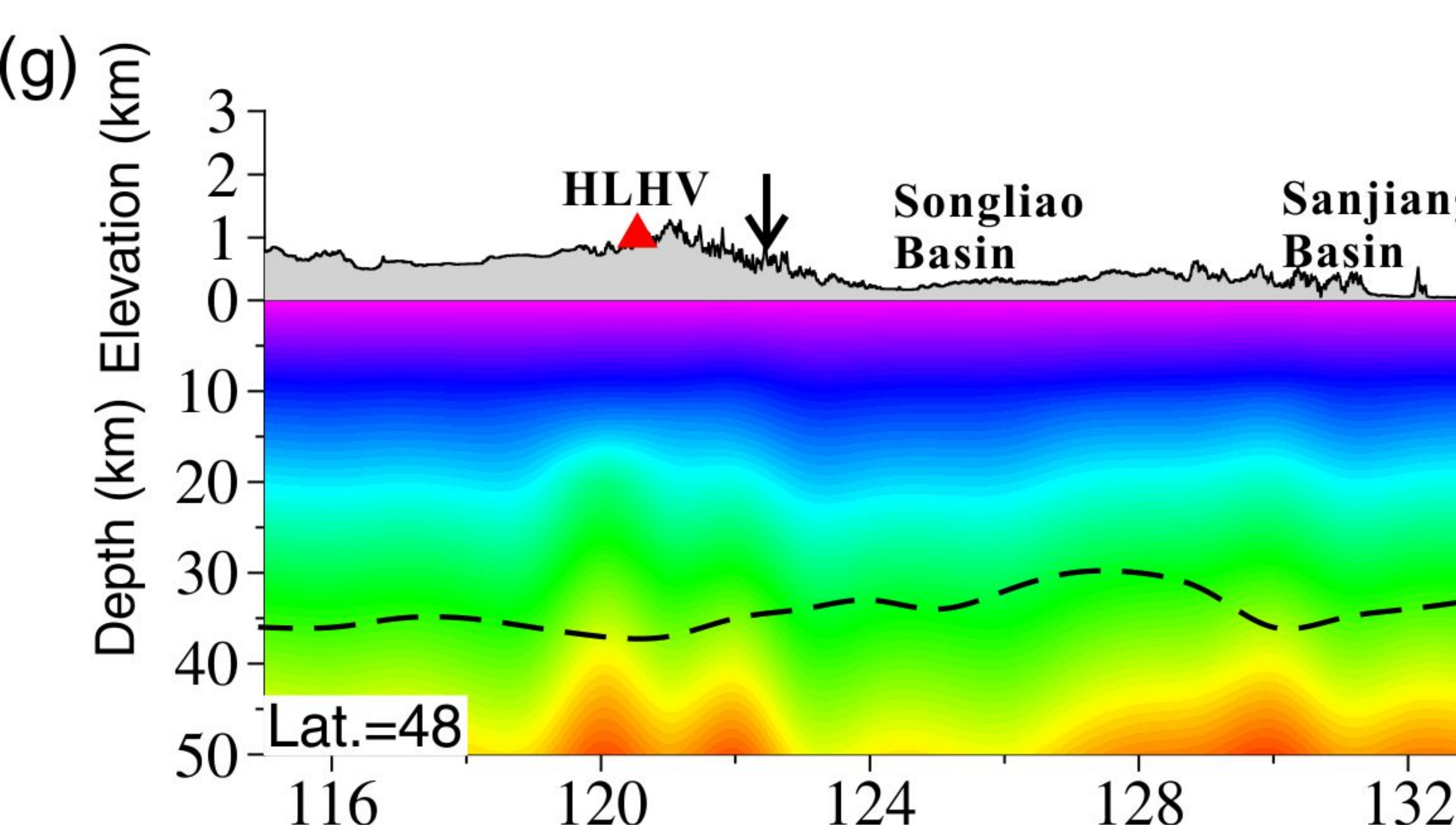
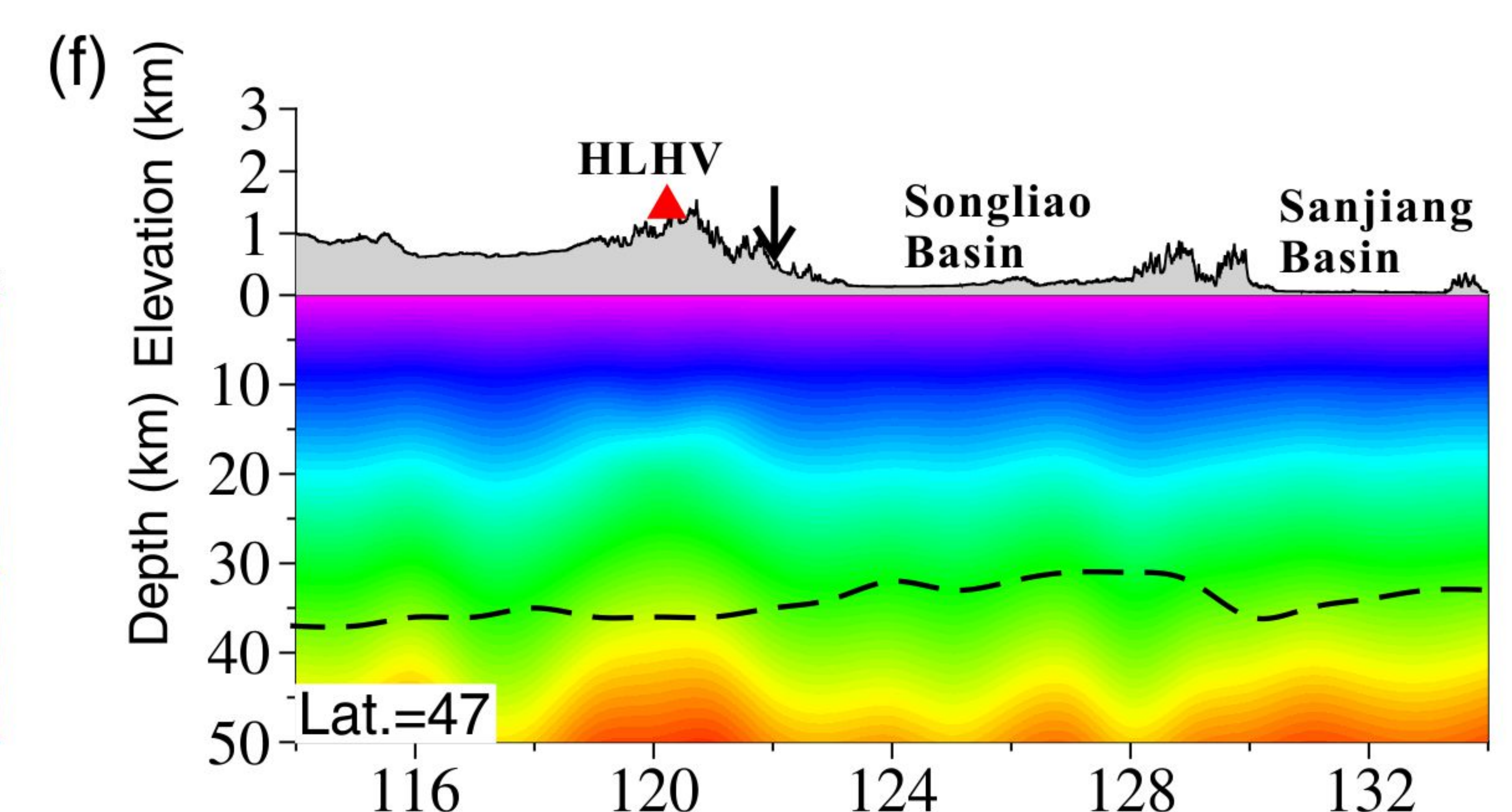
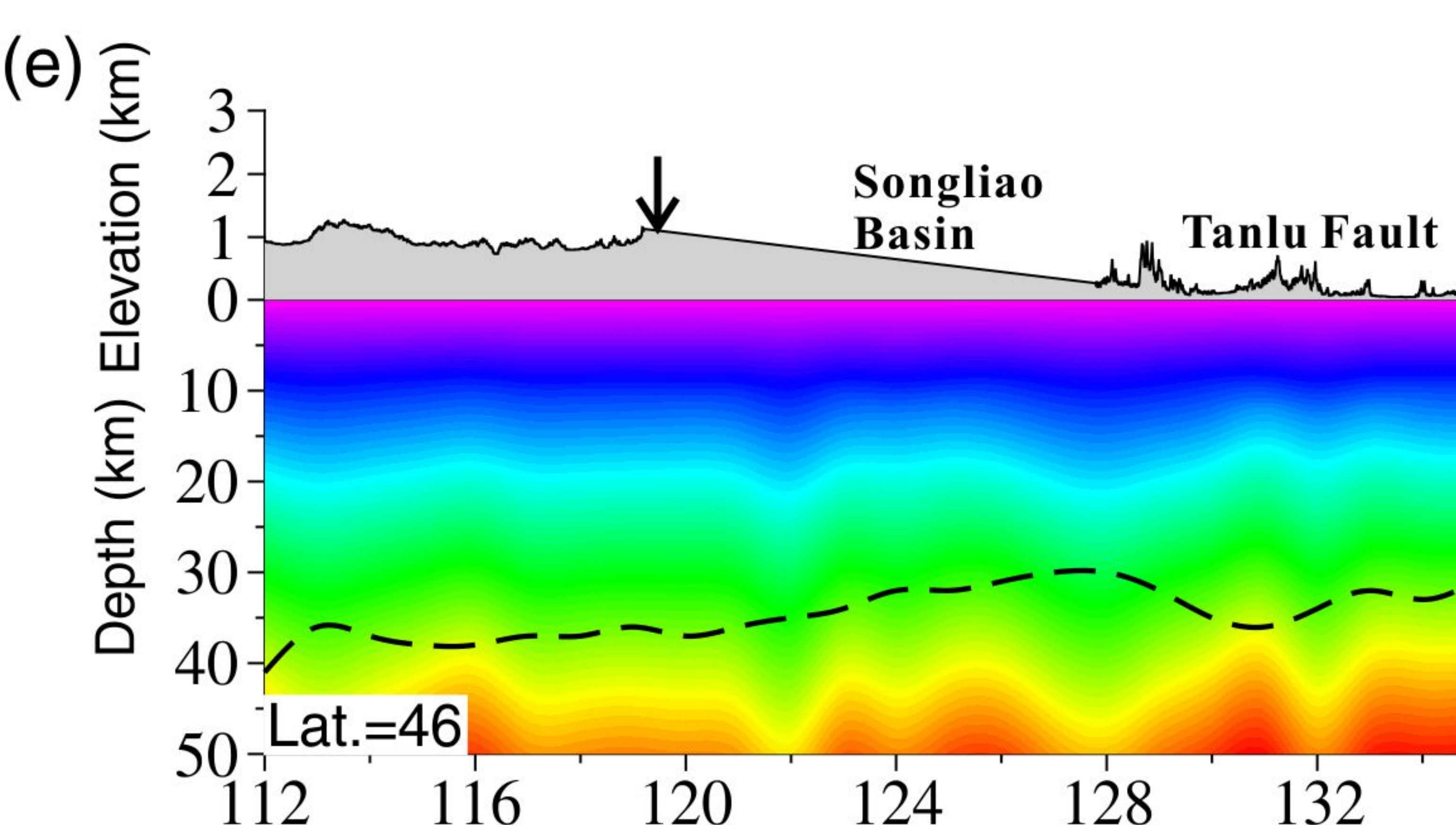
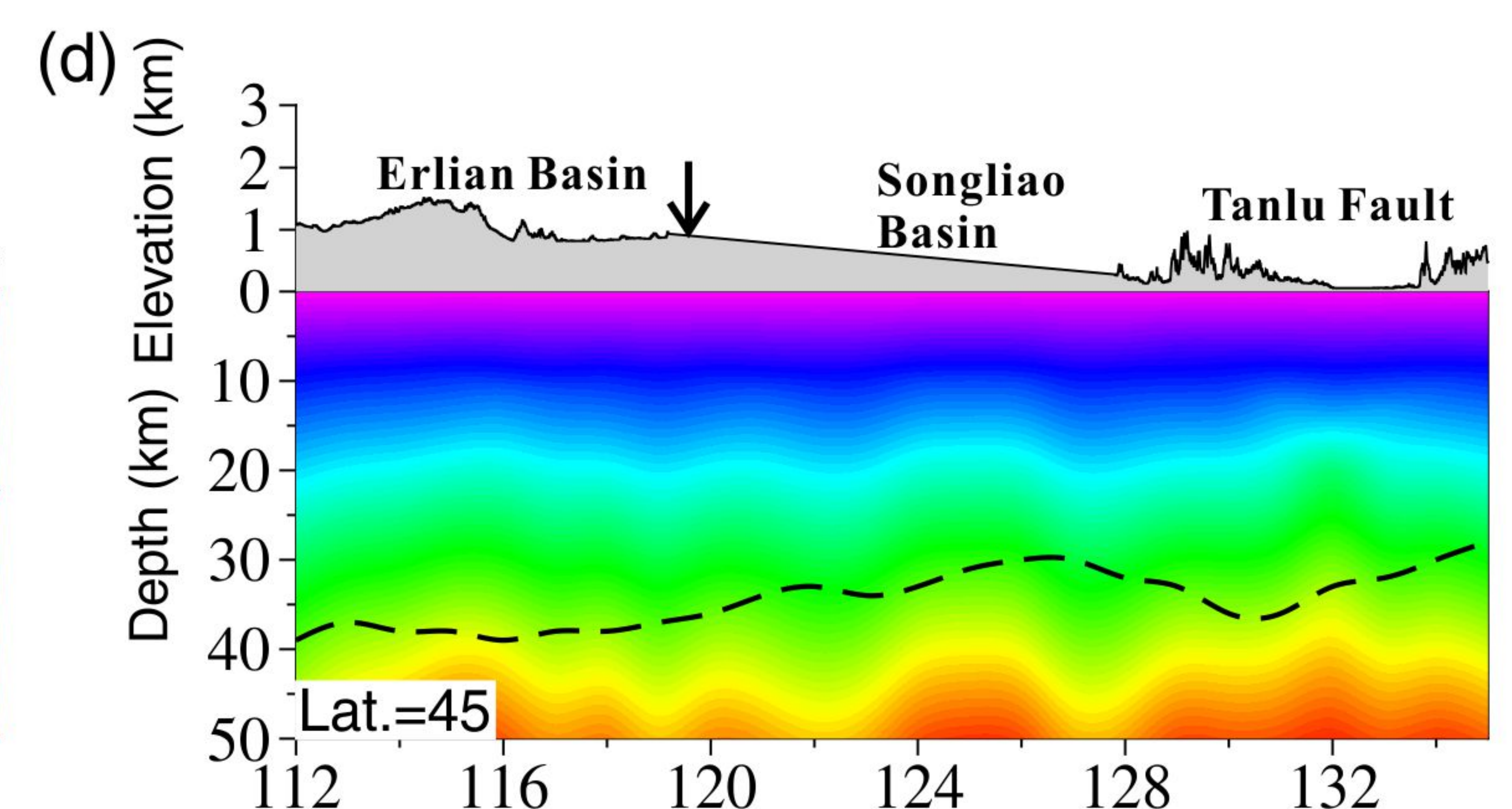
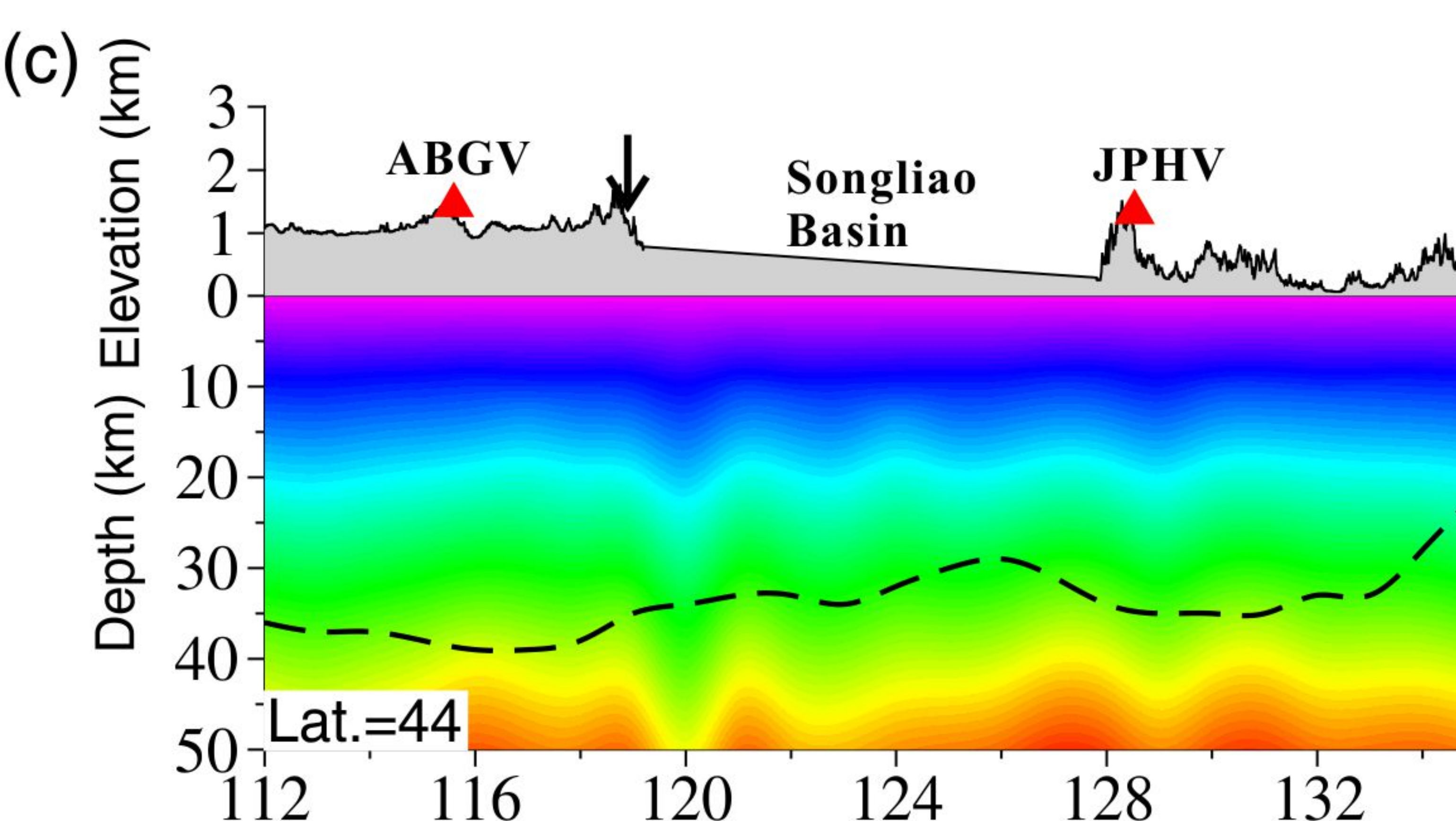
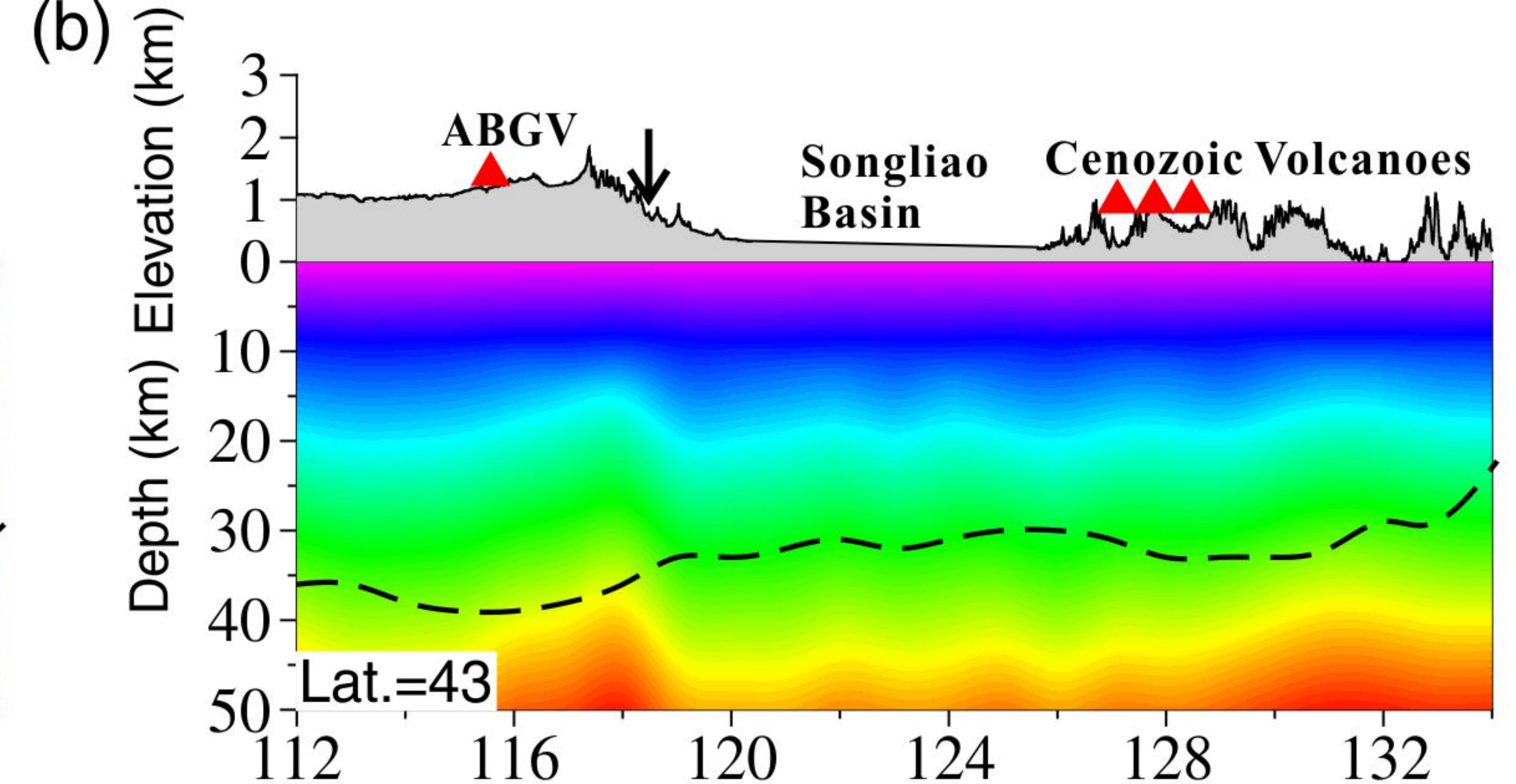
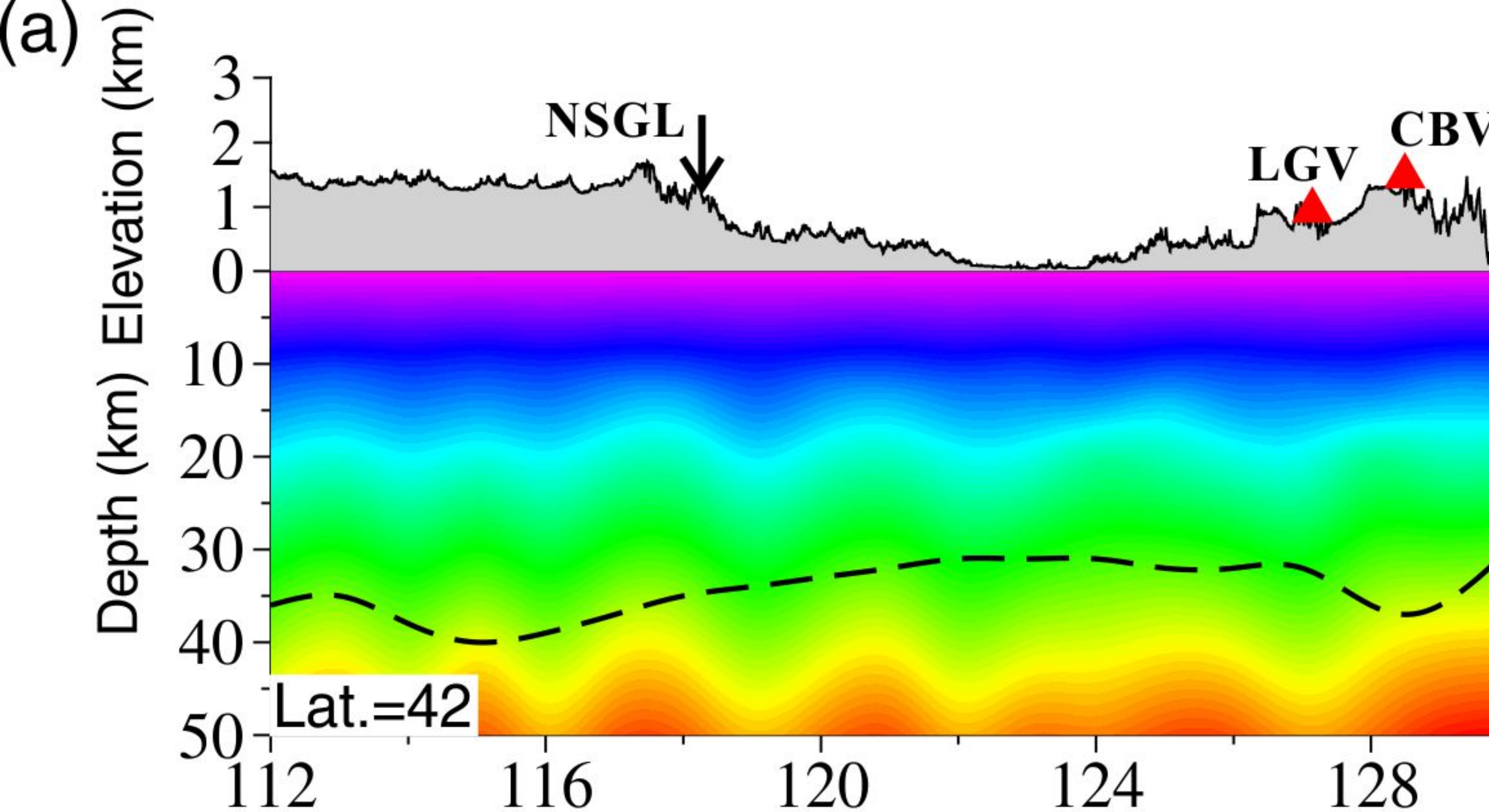


**Figure 5.**

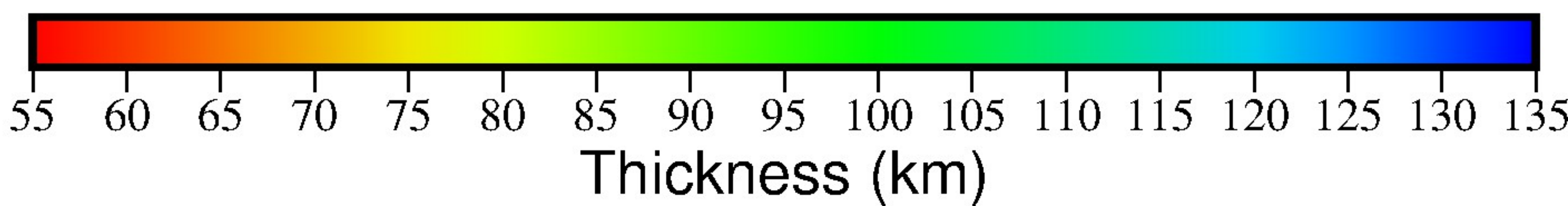
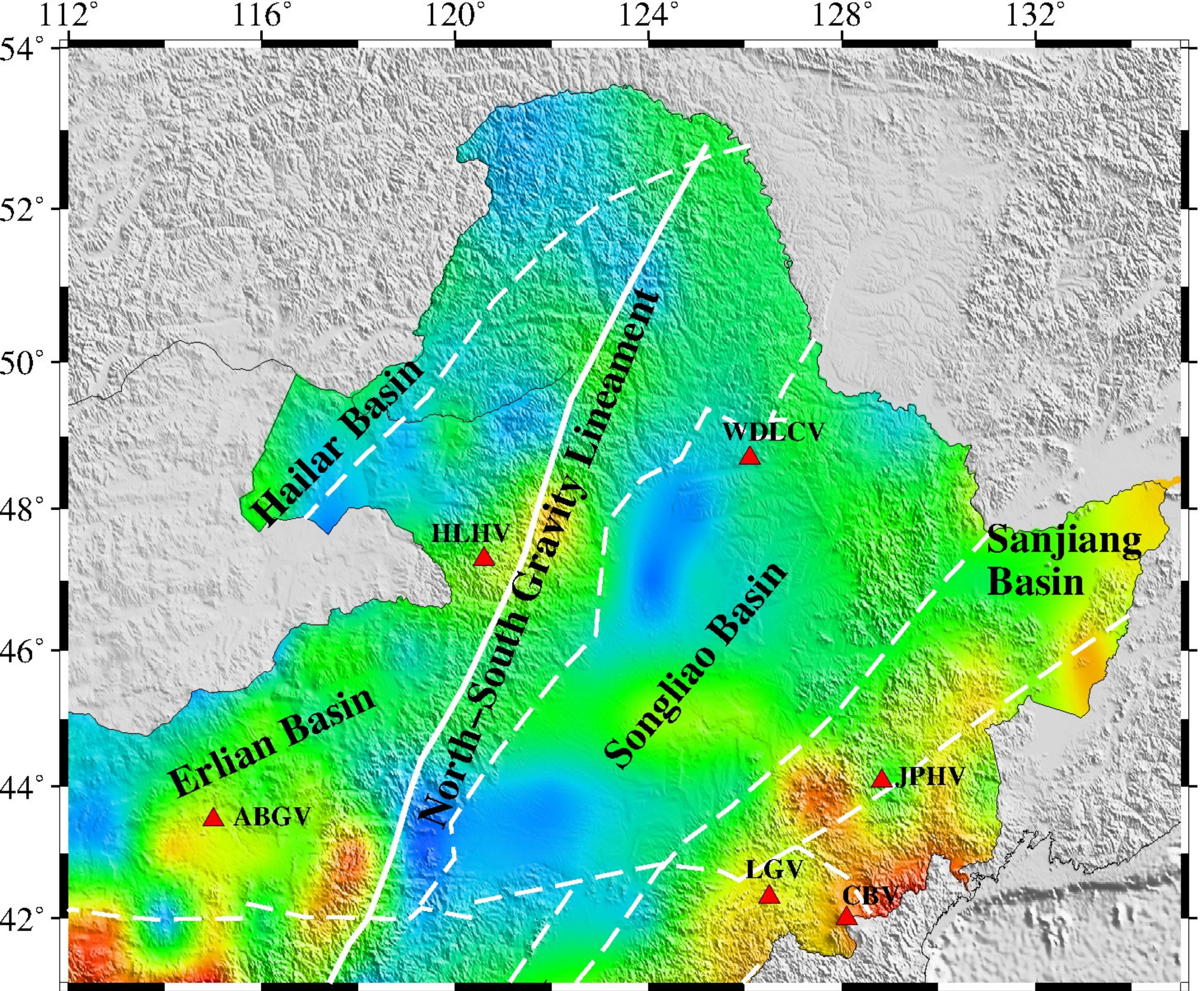
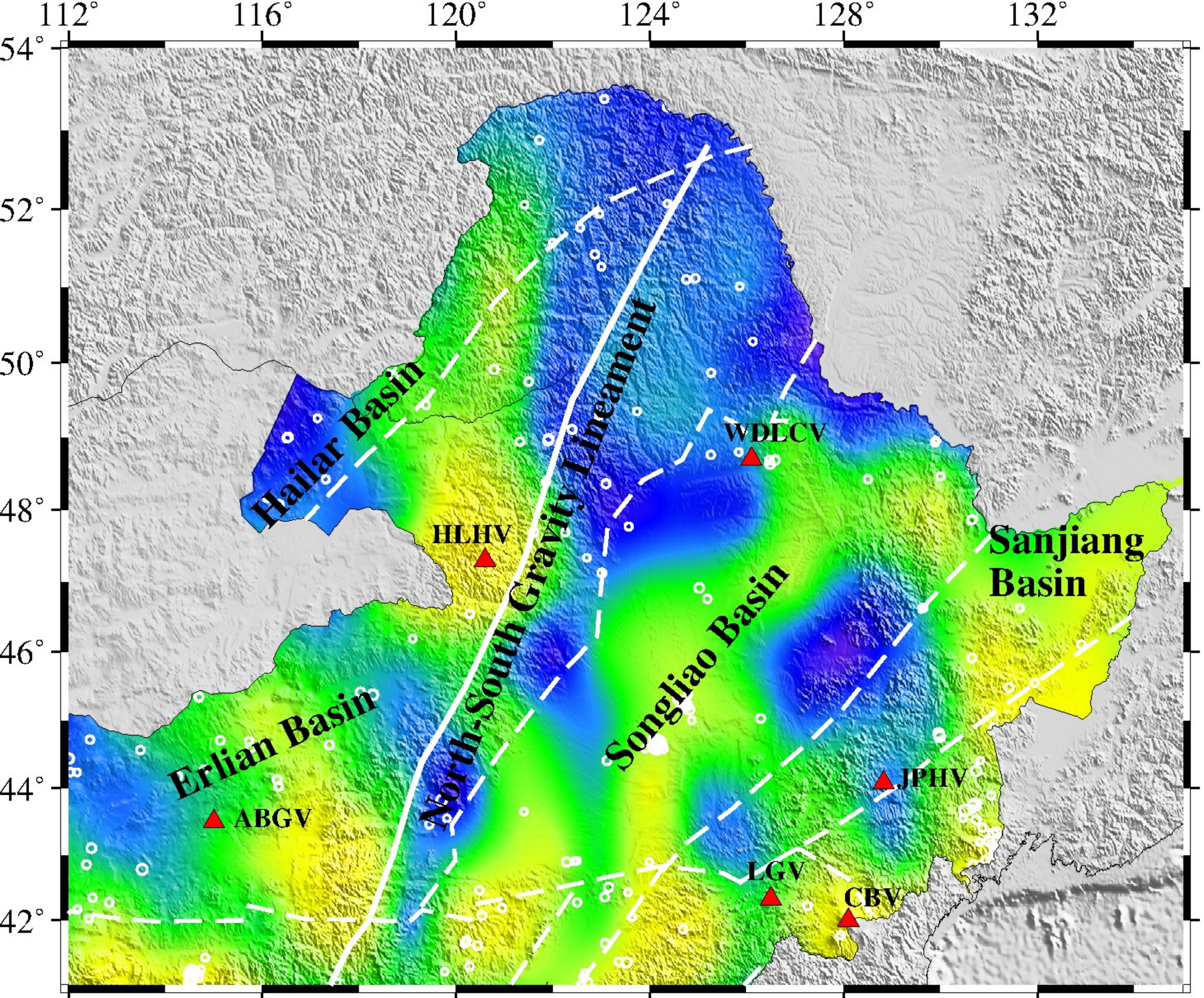


**Figure 6.**



Strength ( $10^{12}$  Pa·m)

0.0 0.4 0.8 1.2 1.6 2.0 2.4 2.8 3.2

**Figure 7.**

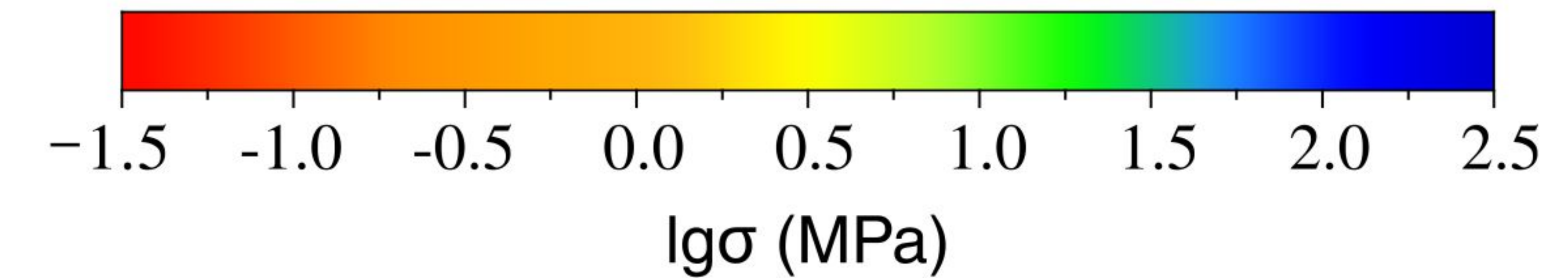
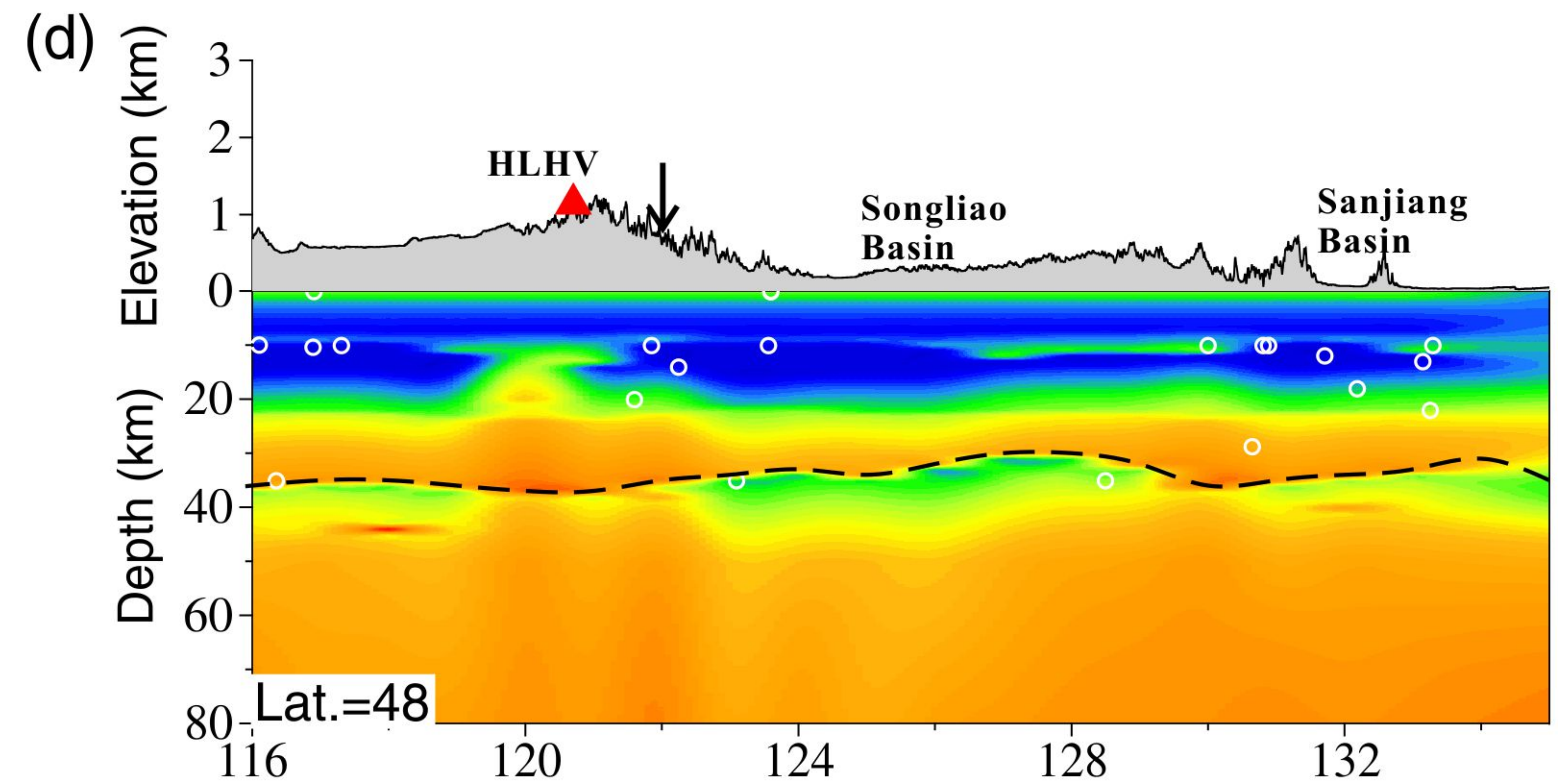
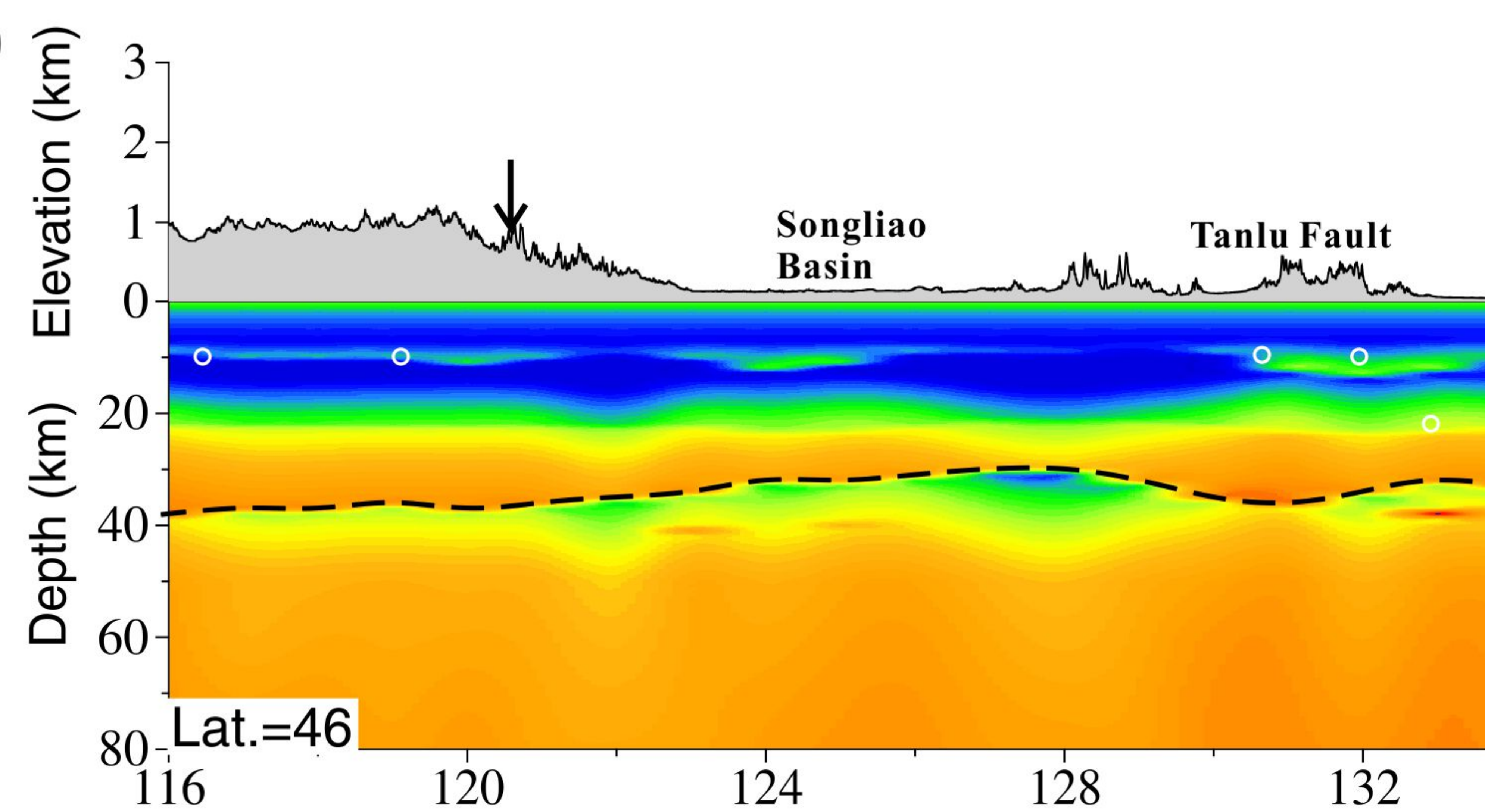
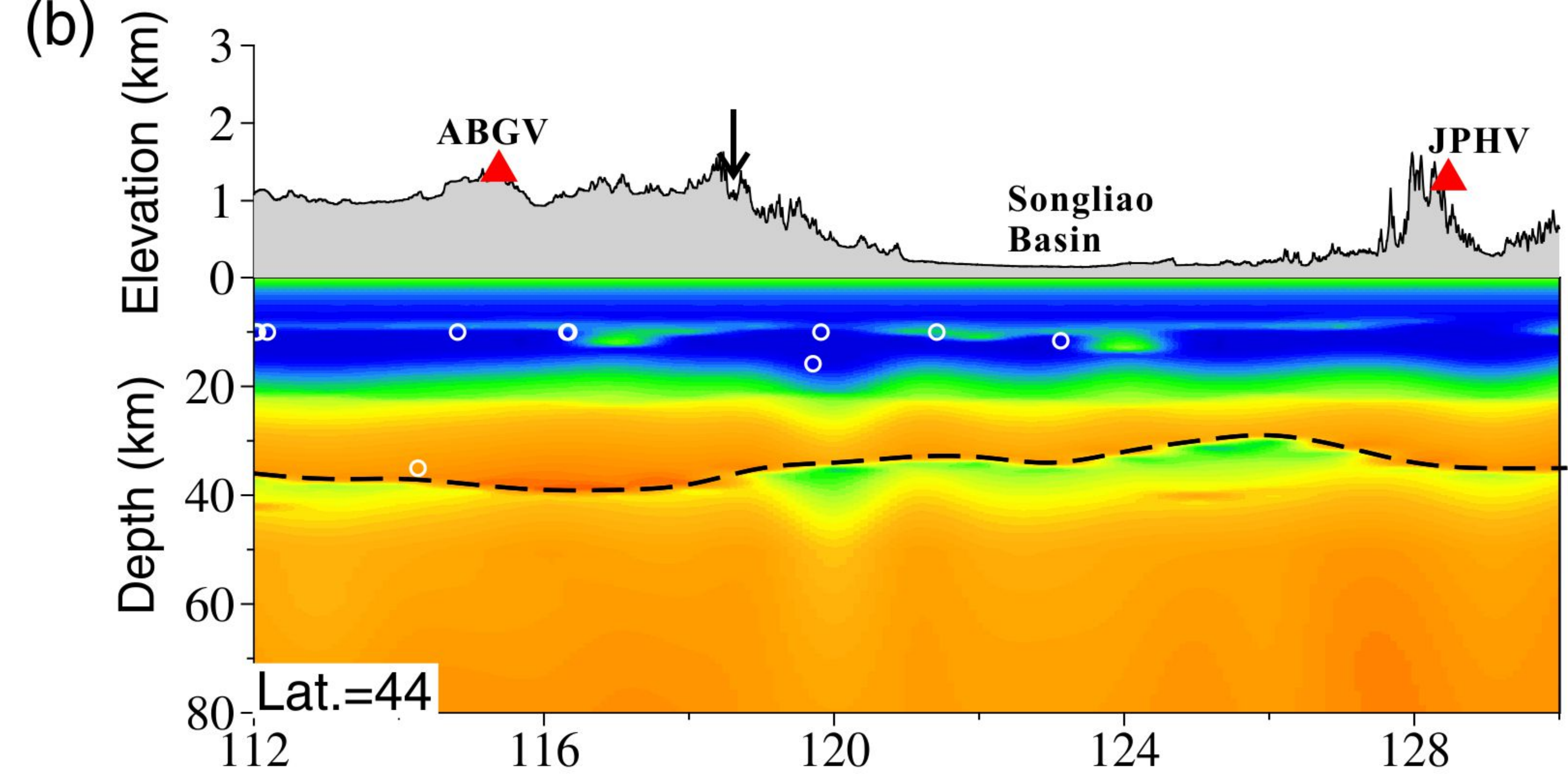
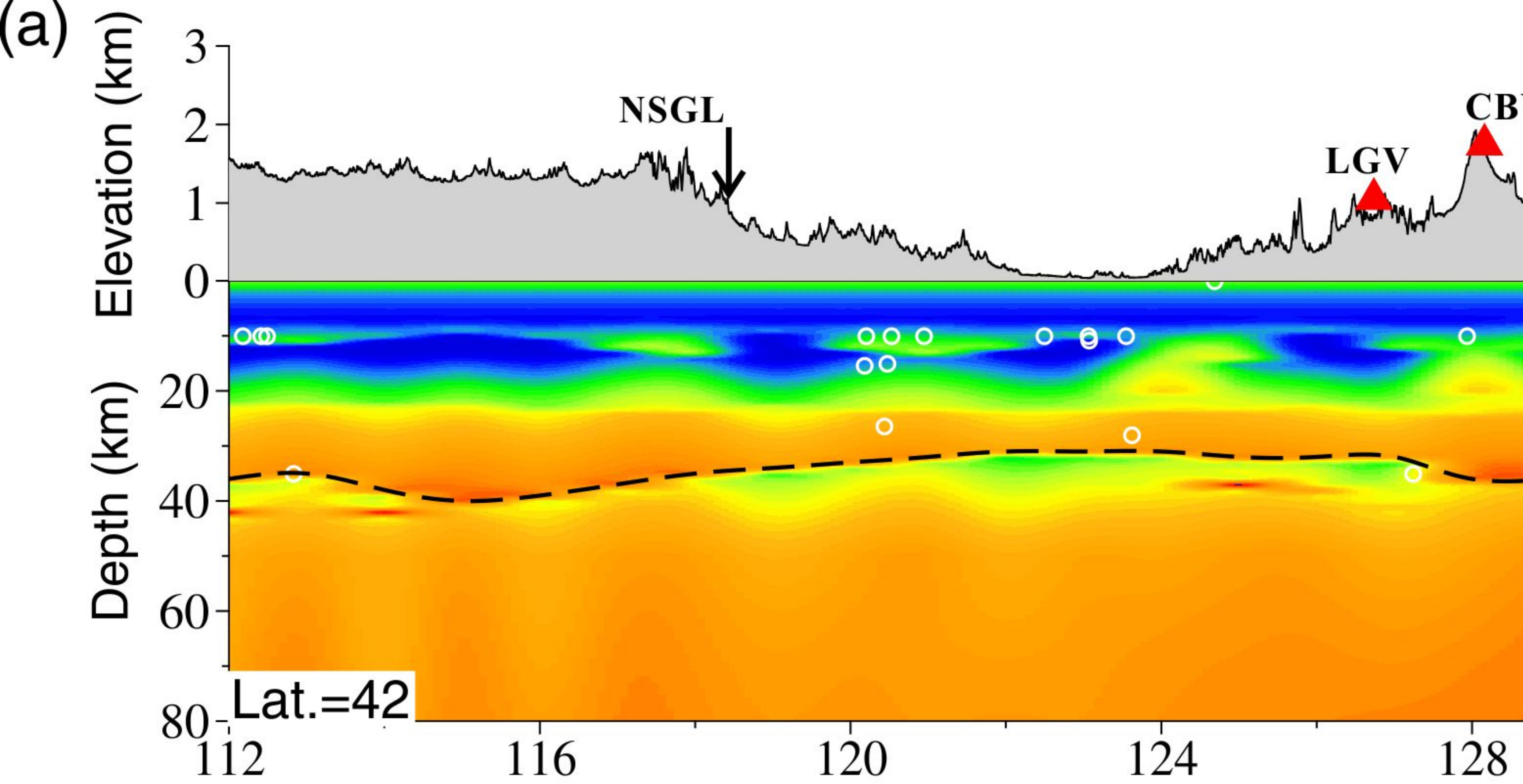


**Figure 8.**

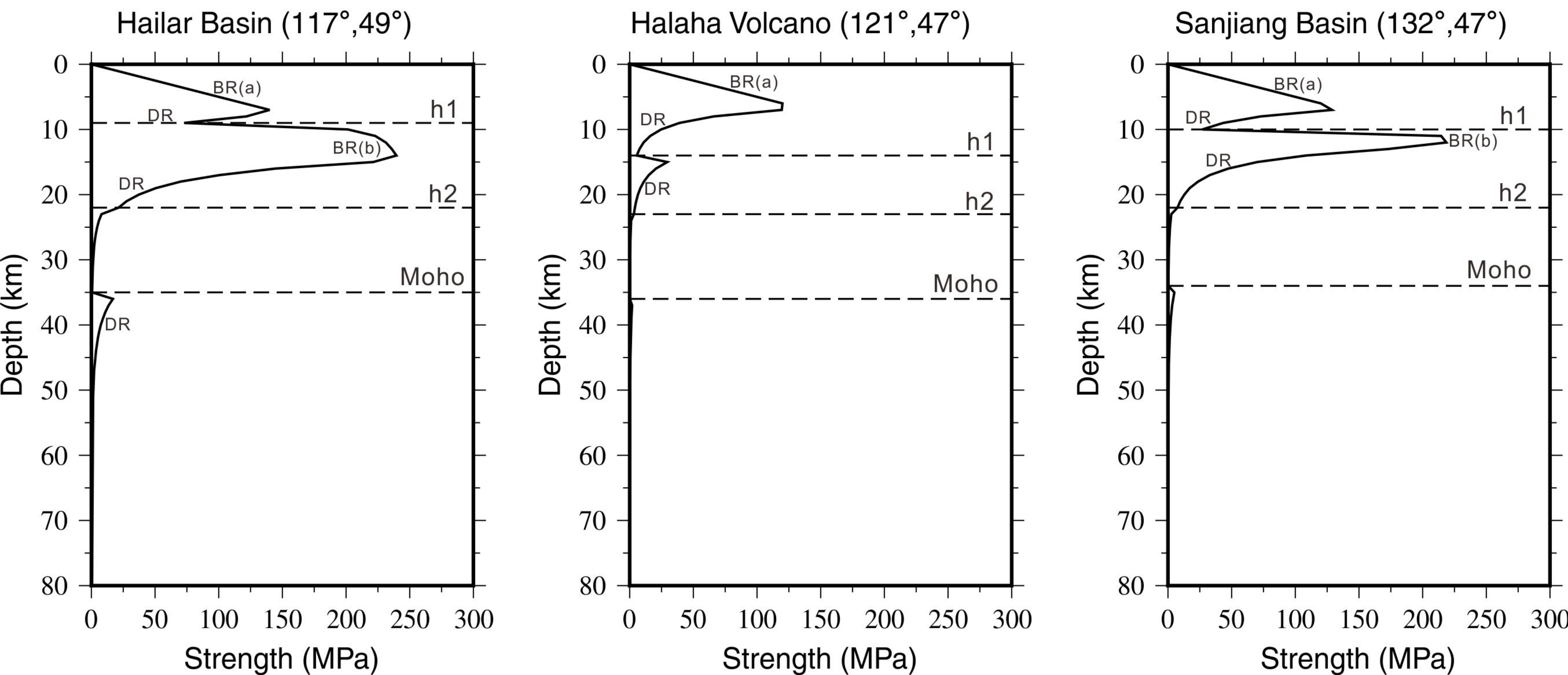
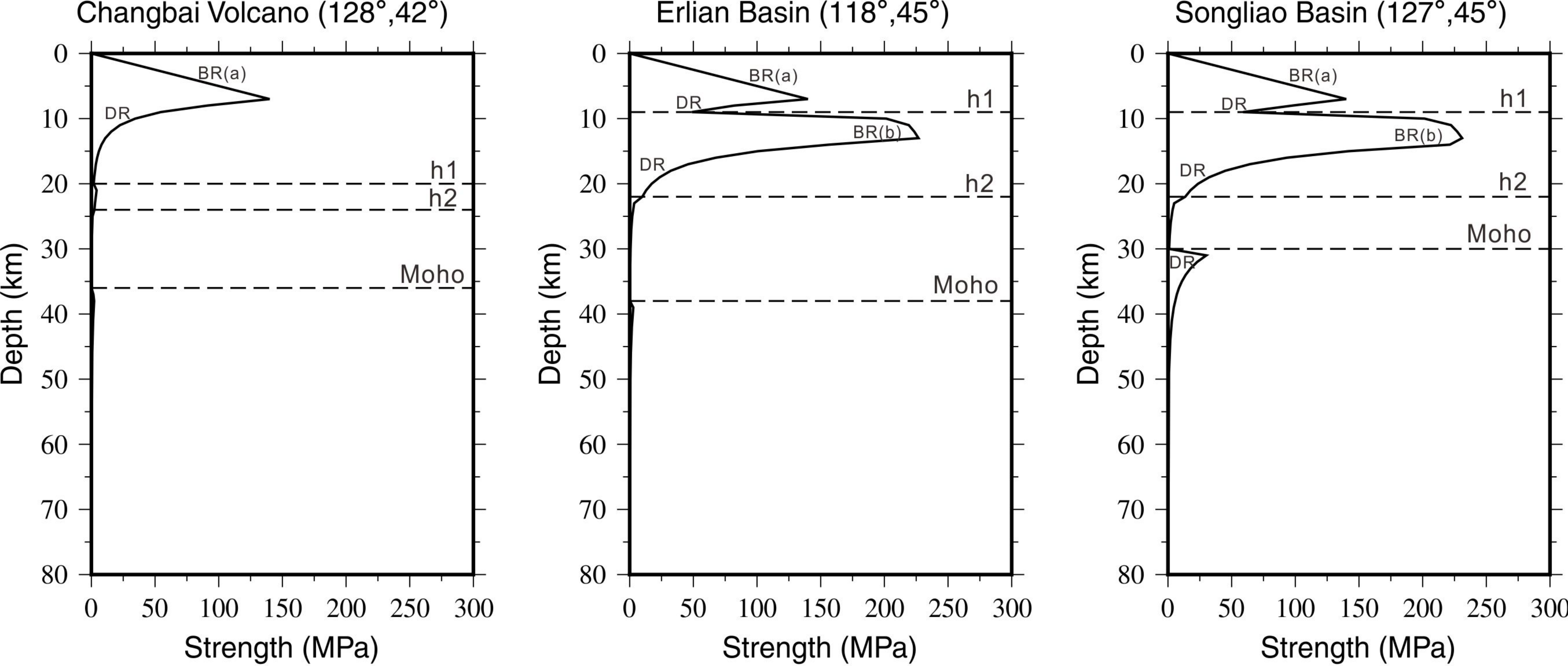


**Figure 9.**

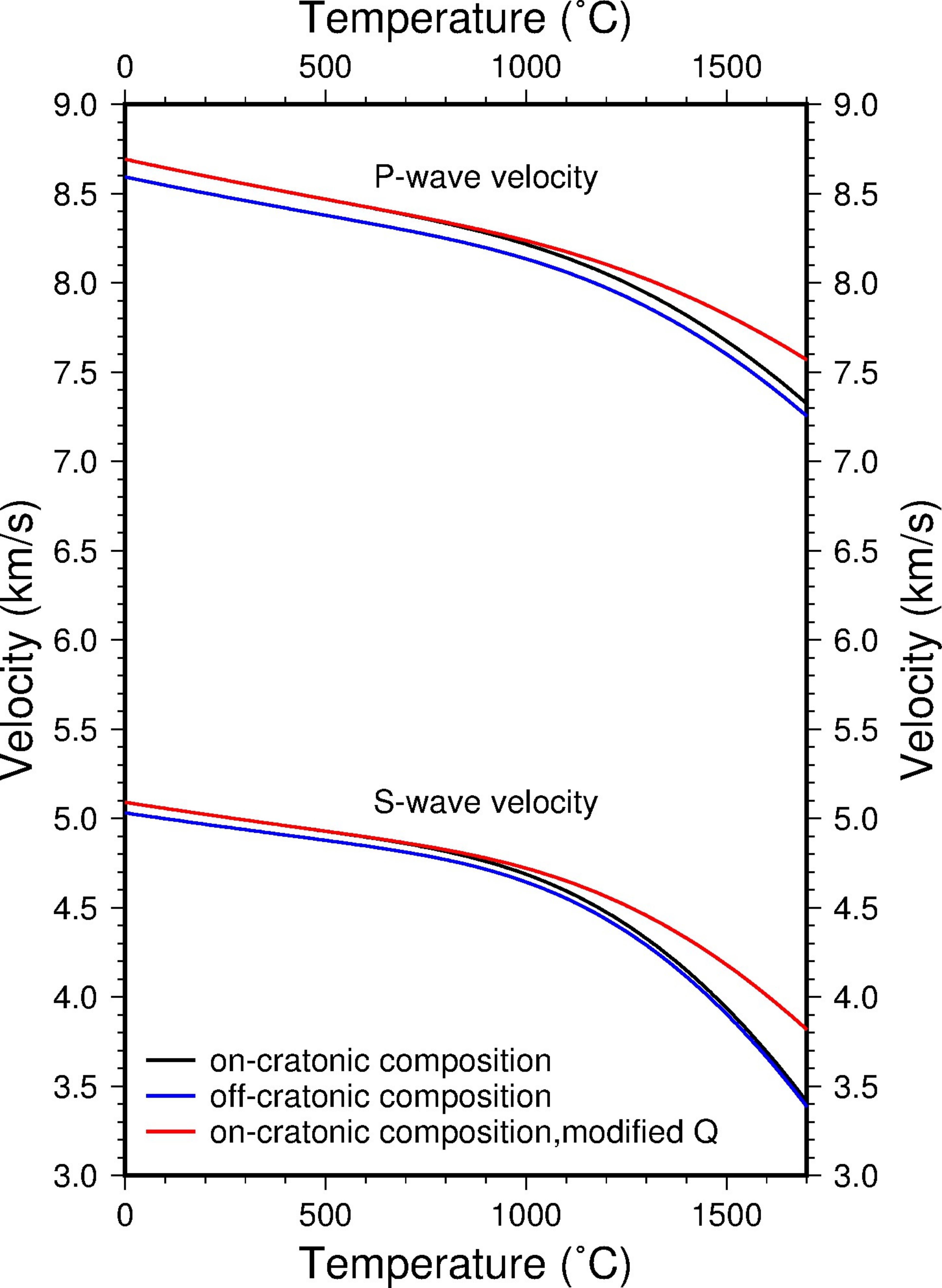


**Figure 10.**

